RUHR-UNIVERSITÄT BOCHUM

RUB

Implementation of COSMO- & PE-PNO-CC2 and their Application to Organic Molecules

Master's Thesis

by
Matthias Rückert
M-Nr. 108008204094

Supervisor: Prof. Dr. Christof Hättig
Ruhr-Universität Bochum
Lehrstuhl für Theoretische Chemie
(Date: 08. October 2019)

Acknowledgements

First of all, I would like to thank Prof. Dr. Christof Hättig for giving me the opportunity to work on the TURBOMOLE code and for being always motivated to help me. It was always a good idea to knock on his office door and wait for the (linear) response "Jaaaaaa", especially when I had questions about the TURBOMOLE code or coupled-cluster theory.
Furthermore, I want to thank my mother Wioletta and my father Martin Rückert, such as my sister Karolina for the outstanding support. Without you I wouldn't survive the first semester of my studies :).
Many thanks also to Marius Frank, Sarah Khani and Alireza Marefat Khah, who were always helpful and available to answer my questions about PNOs, COSMO and PE.

Contents

1 Introduction **1**

2 The Coupled-Cluster Lagrangian Formalism for Solvation Models **4**
2.1 The PE-Lagrangian 5
2.2 The COSMO-Lagrangian 8
2.3 The Ground State COSMO- & PE-CC2 Equations 9
2.4 The COSMO & PE-CC2 Jacobi Matrix 11

3 Pair Natural Orbitals for the ground and excited state **13**

4 Implementation **16**

5 Results **20**
5.1 Computational Details 20
5.2 Accuracy of the Implementation 20
5.2.1 Accuracy of the COSMO-PNO-CC2 Implementation 22
5.2.2 Accurancy of the PE-PNO-CC2 implementation 29
5.3 Performance of the COSMO-PNO-CC2 Implementation 31
5.4 Application of COSMO-PNO-CC2 to Rylenediimides 36
5.4.1 Unsubstituted Rylenes 37
5.4.2 Bay-Substituted Rylenes 39

6 Summary & Outlook **44**

7 Appendix **46**

Abbreviations

AO	Atomic Orbital
ADC(2)	Algebraic-Diagrammatic Construction throug Second Order
CC	Coupled-Cluster
CC2	Second-Order Approximate Coupled Cluster Singles and Doubles Model
CIS	Configuration Interaction Singles
CIS(D)	Second Order Perturbation Correction to CIS
CSM	Continuum Solvation Model
COSMO	Conductor-Like-Screening Model
DFT	Density Functional Theory
HF	Hartree-Fock
MP2	Second Order Møller-Plesset Perturbation Theory
OSV	Orbital Specific Virtual
PAO	Projected Atomic Orbital
PCM	Polarizable Continuum Model
PE	Polarizable Embedding
PNO	Pair Natural Orbital
PTE	Perturbation through Energy Reaction Field
PTED	Perturbation through Energy and Density Reaction Field
RI	Resolution-of-the-Identity

1 Introduction

The linear response formalism in combination with an exponential parametrization of the wavefunction[1–3], as used in coupled-cluster (CC) theory[4–7], is an accurate machinery for the prediction of electronic spectra of chromophores in vacuum, especially when considering higher excitation classes within the ground state wavefunction ansatz. Thus, the CC3[8] method that includes connected triples cluster amplitudes predict excitation energies with an intrinsic methodic error of $\sim 0.01\,\mathrm{eV}$[9], which lies under the magic mark of chemical accurancy $\sim 0.04\,\mathrm{eV}$. However, coupled-cluster methods in their canonical formulation suffer from an high time complexity. Depending on the approximation made in terms of truncation of the exponential parametrization and inclusion of specific terms that are correct to a certain order in the fluctuation potential, the computational costs can be estimated to: CCS ($\mathcal{O}(\mathcal{N}^4)$), CC2[10] ($\mathcal{O}(\mathcal{N}^5)$), CCSD[5] ($\mathcal{O}(\mathcal{N}^6)$), CC3[8] ($\mathcal{O}(\mathcal{N}^7)$), CCSDT[6] ($\mathcal{O}(\mathcal{N}^8)$). The steep scaling within the coupled-cluster hierarchy results in the fact, that the CCSDT approach is only applicable to small molecules.
A computational less elaborate approach to excitation energies can be achieved by combining density functional theory[11,12] (DFT) with the linear response scheme. However, within DFT correlation effects are captured in the exchange-correlation functional, whose mathematical form is unknown and thus has to be approximated, mostly by functionals, that are fitted to experimental data or contain contributions of the exact Hartree-Fock (HF) exchange energy.[13] Therefore, no systematical incorporation of correlation effects is possible, like in coupled-cluster theory. The weakness of DFT to approach dynamic correlation effects results in the necessity to include correction terms for the description of weak intermolecular interactions, as dispersion effects.[14,15] Furthermore, the description of non-local excitation processes turns out to be problematic within TDDFT, leading to the development of special range-separated hybrid functionals like CAM-B3LYP[16], that also tend to overestimate transition energies.[17] Thus developing low-scaling variants of high-accurate coupled-cluster methods is of particular importance and a lot of research was devoted to achieving this task.
The high computational complexity of CC methods in their canonical parametrization is rooted in the fact that all possible combinations of electron pairs, triples ... etc. are included within the correlation treatment. However, it is well known that electron correlation scales as $\mathcal{O}(\mathcal{R}^{-6})$ with the interelectronic distance[18], and thus very distant pairs do not significantly contribute to the ground state correlation energy. Thus the num-

ber of significant electron pairs increases linearly with the system size, leading to the possibility to reduce the space of double, triple ... etc. cluster amplitudes and thus the scaling of CC schemes. Especially methods that are based on the truncation of the virtual space, as it was first introduced by Pulay and Sabøe[19–25], lead to efficient and low-scaling implementations of coupled-cluster methods.[26–28]

These low-scaling approaches make use of a tensor factorization of the doubles space[29], in the sense that they represent the virtual space by projected atom orbitals[19,20] (PAOs), orbital specific virtual orbitals[29] (OSVs) or pair natural orbitals[30] (PNOs). In this connection, PNOs give rise to the most compact virtual space since each pair of occupied molecular orbitals is mapped to an individual set of PNOs, which represent a pair specific virtual space. However, since the generation of OSVs and PAOs are less elaborate, hybrid schemes were developed to achieve an efficient PNO construction. Hättig *et al.* downscale the PNO construction, that is based on the MP1 one-electron density ($\mathcal{O}(\mathcal{N}^5)$, by a hybrid OSV-PNO scheme to $\mathcal{O}(\mathcal{N}^3)$.[31] Extending the ground state OSV-PNO approach to excited states in the framework of linear response theory, Helmich *et al.* constructed state-specific excited state PNOs, by using a one-electron density based on excited state doubles amplitudes obtained by CIS(D) calculations.[32,33] This scheme was extended to the CC2[26] and CCSD[27] approach for gas-phase excitation energies. Similar efforts were conducted with the use of a PAO-PNO hybrid scheme by Neese *et al.*, by combining this scheme with the CCSD approach[28] for ground state properties.

Besides the reduction of the time complexity of the quantum mechanical method itself, the computational costs can be reduced by minimizing the number of molecules taken into account within the quantum mechanical treatment. This becomes of particular importance when solvent or other environmental effects have to be studied. Here, two main approaches are followed. The first one retains an atomistic representation of the environment by means of a distribution of static and polarizable multi moments, such as additional terms, like dispersion potentials. Especially, for excitation processes, a polarizable field is of particular importance[34], to represent the response of the electronic structure of the environment to the change of the electronic structure of the solute upon excitation. Thus polarizable embedding (PE) schemes were developed for TDDFT[35] and within coupled-cluster response theory, like the PE-RI-CC2 scheme for excitation energies[36] and two-photon absorptions[37], the PE-CCSD method for transition energies[38], such as the PE-ADC(2) scheme for excited state gradients.[39] The second way to describe solute/solvent interactions efficiently is to represent the solvent as a polarizable continuum, as done in continuum solvation models (CSM).[40] Within the CSMs the solvent response to the QM charge density is mapped on a polarizable surface, which is constructed based on the molecular structure of the solute. Depending on the boundary condition used to obtain the surface charges, different variants of CSMs were obtained, like the polarizable continuum model[41] (PCM), such as the conductor-like continuum

model[42] (COSMO). Both were combined with coupled-cluster response theory for the computation of solvation effects on excitation energies. The PCM scheme was combined with the CCSD model for ground state energies[43,44], such as excitation energies[45] and excited state gradients[46] by Caricato. The COSMO approach was combined with ADC(2) by Lunkenheimer and Köhn[47] for transition energies and was extended for excitation energies to the CC2 model, such as for the evaluation of excited state gradients within the ADC(2) scheme by Karbalaei Khani *et al.*.[48]

For correlated wavefunction-based methods, the correlation contribution to the mutual polarization between the solute and the solvent can be treated in different ways. Starting with molecular orbitals, which already contain polarization contributions on the HF level of theory, two main approaches can be identified. Neglecting correlation contributions to the polarization leads to the perturbation through energy scheme[49] (PTE), while a full self-consistent treatment of this effect can be realized with the perturbation through energy and density[49] (PTED) approach. The PTED method is connected with a high computational effort since self-consistency is achieved by a loop over HF and post-HF methods. Therefore intermediate schemes were developed in which this loop is avoided and only the singles excitation parts of the wavefunction parameter contribute to the mutual polarization, as it was introduced by Caricato in his PCM-CCSD implementation[44] and used by Hättig *et al.* in a similar way to maintain the efficiency of the RI-CC2 scheme in the framework of polarizable embedding.[36] As it was shown, this reaction field describes the largest portion of the correlation contribution to the mutual polarization.[44] Recently, this scheme, which was named post-SCF reaction field, was also introduced in the COSMO-RI-CC2 implementation by Karbalaei Khani*et al.*[48]

A natural next step in the development of efficient coupled-cluster approaches for the computation of absorption spectra within linear response theory is to combine both branches, that is a low-scaling coupled-cluster schemes that exploit the local character of electron correlation and solvation models that describe the influence of solvation to the electronic structure of the solute in a way that no or only a few solvent molecules have to be treated by the QM method. Thus, this thesis aims to combine the PNO-CC2[26] scheme with the conductor-like screening model[42], such as the polarizable embedding scheme[36] in their post-SCF reaction field[36,48] variants to obtain the COSMO-PNO-CC2 and PE-PNO-CC2 approaches.

This thesis is structured as follows: the most relevant equation for the computation of excitation energies within the COSMO- and PE-PNO-CC2 schemes are presented in chapter 2 and 3, respectively. The implementation is discussed in chapter 4, while the results are presented in chapter 5, followed by the summary and the outlook (chapter 6).

2 The Coupled-Cluster Lagrangian Formalism for Solvation Models

Central for the inclusion of solvation models to cupled-cluster theory is a formulation in terms of an generalized Lagrangian[38,50], in which the vacuum electronic Hamiltonian $\hat{H}^{\mathrm{QM}}$ is augmented by an operator that describes the coupling between the solutes charge density and the environment

$$\mathcal{L} = \langle\Lambda|\hat{H}^{\mathrm{QM}} + \hat{G}^{\mathrm{env}}(\mathbf{D}^{\mathrm{CC}})|\mathrm{CC}\rangle + E^{const}. \tag{2.1}$$

Here the coupled-cluster wavefunction $\Big|\mathrm{CC}\Big\rangle$ is constructed by the usual exponential parametization[4–7]

$$\Big|\mathrm{CC}\Big\rangle = \exp(\hat{\mathrm{T}})\Big|\mathrm{HF}\Big\rangle, \tag{2.2}$$

that includes all possible excitations out of a reference wavefunction. Here the Hartree-Fock single slater determinate $\Big|\mathrm{HF}\Big\rangle$ was used as reference wavefunction, since the following discussion is restricted to systems, whose electronic structure can be qualitatively correct described by a single slater determinate. The cluster operator

$$\hat{\mathrm{T}} = \sum_{i}^{N} \hat{\mathrm{T}}_i \tag{2.3}$$

$$= \sum_{i}^{N} \sum_{\mu_i} t_{\mu_i} \hat{\tau}_{\mu_i} \ , \tag{2.4}$$

generates all possible excitations $\{\mu_i\}$ for a given excitation order i, where the maximal excitation order equals the total number of electrons N. Truncating the cluster operator after a certain excitation order lead to the hierarchy of coupled-cluster methods. For example, the coupled-cluster singles and doubles method[5] (CCSD) can be optained by truncating the cluster operator after double excitations ($\hat{T} = \hat{T}_1 + \hat{T}_2$). Together with the definition of equation 2.2, the whole set of cluster amplitudes $\{t_{\mu_i}\}$ define the coupled-

cluster wavefunction. The Schrödinger equation in equation 2.1 is projected onto an auxiliary state

$$\Big\langle\Lambda\Big| = \Big\langle\mathrm{HF}\Big| + \sum_{\mu_i} \bar{t}_{\mu_i}\Big\langle\mu_i\Big|\exp(-\hat{\mathrm{T}}) \ , \tag{2.5}$$

that includes a dependence on the lagrange multipliers $\{\bar{t}_{\mu_i}\}$ and the whole excitation manifold $\{\Big\langle\mu_i\Big|\}$.
The environmental coupling operator $\hat{G}^{\mathrm{env}}(\mathbf{D}^{\mathrm{CC}})$ can have an explicit dependency to the solutes charge density, if the solvation model includes the possibility that the solvent can respond to the QM charge density, for example, in terms of polarizable sites. The mutual polarization between the QM part and the solvent give rises to a reaction field. The post-SCF reaction field[36,48] that is used in this thesis is described in more detail in section 2.3. In contrast to the vacuum case, an explicitly $\mathbf{D}^{\mathrm{CC}}$-dependent coupling operator lead to coupled equations for the ground state cluster amplitudes and Lagrange multiplier (see section 2.3), since the unrelaxed coupled-cluster density is constructed by both parameters t_{μ_i} and $\bar{t}_{\mu_i}$, respectively Using the spin-free one-particle operator[51] $\hat{E}_{pq}$, the coupled-cluster density matrix elements are defined in second quantization as,

$$D^{\mathrm{CC}}_{pq} = \langle\Lambda|\hat{E}_{pq}|\mathrm{CC}\rangle. \tag{2.6}$$

In the following two sections, the conductor-like screening model and the polarizable embedding approach are discussed together with their Lagrangian and environmental coupling operator.

2.1 The PE-Lagrangian

Within general PE-CC theory[38] the system of interest is split into a QM and a MM region. The QM part is described by coupled-cluster methods, wherease the MM subsystem is build of permanent and polarizable multipoles, which are placed at MM sites s and u, respectively. In general, multi moments of arbitrary order $Q^{(k)}$ can be incoorperated in this approach, where the superskript k denotes the order of the multipole, i.e. k=0 is a point chagre, k=1 is a dipole moment, and so on. However, the following discussion is restricted to the current implementation of the PE-CC[36] approach within the `TURBOMOLE` program package[52], which includes permanent multipoles up to quadrupoles such as polarizable dipole moments.
In the PE-CC2[36] approach the QM charge density can interact with k-th order multipoles. In order to simplify the notation of these interactions a tensor formalism[53] is advantageous. This formalism has its origin in a multipole expansion of the potential steaming from the MM subsystem and it facilitate the introduction of an effective oper-

ator that return the potential for the components $\gamma_1\gamma_2\ldots\gamma_k$ ($\gamma = (x, y, z)$) of the k-th order multipole at MM site s due to the electronic density

$$\hat{\varepsilon}_{s\gamma_1\gamma_2\ldots\gamma_k} = \sum_{pq} \varepsilon_{pq}^{s\gamma_1\gamma_2\ldots\gamma_k} \hat{E}_{pq}. \tag{2.7}$$

Here, the matrix elements $\hat{\varepsilon}^{s\gamma_1\gamma_2\ldots\gamma_k}$ are the electron-multipole interaction integrals

$$\epsilon_{pq}^{s\gamma_1\gamma_2\ldots\gamma_k} = \frac{(-1)^{k+1}}{k!} \langle \phi_p(\mathbf{r}_i) | \mathbf{T}^{is}_{\gamma_1\gamma_2\ldots\gamma_k} | \phi_q(\mathbf{r}_i) \rangle, \tag{2.8}$$

that include the correct distance dependence for the interaction of the components of the k-th orde multipole with an electron through the incorporation of the tensor of k-th order

$$\mathbf{T}^{is}_{\gamma_1\gamma_2\ldots\gamma_k} = \nabla^s_{\gamma_1} \nabla^s_{\gamma_2} \ldots \nabla^s_{\gamma_k} \frac{1}{|\mathbf{r}_s - \mathbf{r}_i|}, \tag{2.9}$$

that is the k-th derivative of the coulomb metric with respect to the cartesian components γ of the MM site vector $\mathbf{r}_s$, while $\mathbf{r}_i$ depict the electron coordinate vector. For reasons of readability it is benefitial to include all informations about the multipole components in the MM site indices, e.g. $(s, \gamma_1\gamma_2\ldots\gamma_k) \rightarrow s$.
The PE-CC2 Lagrangian[36] for the system described above, i.e. whose polarizable sites contain dipole moments only, is given by

$$\begin{aligned} \mathcal{L}_{\mathrm{PE}} = &\langle \Lambda | \hat{H}^{\mathrm{QM}} + \hat{G}^{\mathrm{es}} | \mathrm{CC} \rangle \\ &- \frac{1}{2} \sum_u (F_u^{ne} + F_u^{elec}(\mathbf{D}^{\mathrm{CC}})) \mu_u^{\mathrm{ind}}. \end{aligned} \tag{2.10}$$

Besides the contribution from the vaccum Hamiltonian, the Lagrangian contains electrostatic and polarization contibutions. The electrostatic contributions, that is the interaction of the QM electronic density with the permanent multipoles, are represented by the electrostatic coupling operator

$$\hat{G}^{\mathrm{es}} = \sum_s Q_s \hat{\varepsilon}_s. \tag{2.11}$$

By using the definitions of equations 2.6 and 2.8, the matrix elements of the $\hat{G}^{\mathrm{es}}$ operator can be rearranged in a way which makes the coupling between the coupled-cluster electronic charge distribution and the multipoles more apparent

$$\begin{aligned} \langle \Lambda | \hat{G}^{\mathrm{es}} | \mathrm{CC} \rangle &= \sum_s \sum_{pq} Q_s \varepsilon^s_{pq} \langle \Lambda | \hat{E}_{pq} | \mathrm{CC} \rangle \\ &= \sum_{pq} G^{es}_{pq} D^{\mathrm{CC}}_{pq}. \end{aligned} \tag{2.12}$$

The last term in equation 2.10 depict the polarization energy of the induced dipole moments μ^{ind}, that is the energy to create them, such as the energy of these induced moments in the total electric field.[38] Here, F_u^{ne} and $F_u^{elec}(\mathbf{D}^{\text{CC}})$ are the components of the static nonelectronic and electronic contribution to the total electric field, respectively. The static non-electronic field is composed of the field due to the nuclei of the qm systems and all permanent multipoles. Note, that the electric field due to the induced dipole moments do not appear, since these energy contributions cancel out. For further informations see ref[38].

Finally, dipole moments are obtained by a linear polarization of the polarizable MM sites due to the total electric field

$$\mu_u^{ind}(\mathbf{D}^{CC}) = R_{uv}(F_v^{ne} + F_v^{elec}(\mathbf{D}^{\text{CC}})), \tag{2.13}$$

where the dipole-dipole interactions are included through first-order interaction tensors $\mathbf{T}_\gamma$ that appear as off-diagonal elements whithin the classical response matrix

$$R = \begin{pmatrix} \boldsymbol{\alpha}_1^{-1} & -\mathbf{T}_\gamma^{12} & \cdots & -\mathbf{T}_\gamma^{1U} \\ -\mathbf{T}_\gamma^{21} & \ddots & & \vdots \\ \vdots & & \ddots & \vdots \\ -\mathbf{T}_\gamma^{U1} & \cdots & \cdots & \boldsymbol{\alpha}_U^{-1} \end{pmatrix}^{-1} . \tag{2.14}$$

As diagonal elements the dipole-dipole response matrix contain the inverse of the polarizability tensor $\boldsymbol{\alpha}$. Note that the dipole-dipole interaction tensors, such as the polarizability tensors included in the response matrix are 3x3 matrices.

As apparent from equation 2.10 the polarization energy contains contributions from different sources of the electric field. This allows to seperate the contribution steaming from the QM electron density and to definie the environmental coupling operator which contains the polarization part due to the interaction of the electronic charge density with the induced dipole moments

$$\hat{G}^{\text{pol}}(\mathbf{D}^{CC}) = -\sum_u \mu_u^{ind}(\mathbf{D}^{CC})\hat{\varepsilon}_u \tag{2.15}$$

Performing a similar manipulation as in equation 2.12 lead to the matrix elements of the coupling operator of the polarization contribution

$$\begin{aligned} \langle\Lambda|\hat{G}^{\text{pol}}|\text{CC}\rangle &= \sum_u \sum_{pq} \mu_u^{ind}(\mathbf{D}^{\text{CC}})\varepsilon_{pq}^u \langle\Lambda|\hat{E}_{pq}|\text{CC}\rangle \\ &= \sum_{pq} G_{pq}^{\text{pol}} D_{pq}^{\text{CC}}. \end{aligned} \tag{2.16}$$

The final PE-coupling operator is given as the sum of the electrostatic and polarizable coupling operator

$$\hat{G}_{\mathrm{PE}}(\mathbf{D}^{\mathrm{CC}}) = \hat{G}^{\mathrm{es}} + \hat{G}^{\mathrm{pol}}(\mathbf{D}^{\mathrm{CC}}) \tag{2.17}$$

2.2 The COSMO-Lagrangian

Continuum solvation models specify solvents by characteristic macroscopic properties like the relative permitivity ϵ_{r} and the refractive index n_{D}.[40] Furthermore, the individual solvent molecules are replaced by an infinite continuum. Within this continuum, a molecule-shaped cavity is constructed by the overlap of all atom-centered spheres with roughly 120 % of the atomic van der Waals radius.[54] The whole solvent response to the solutes total charge distribution is mapped on the polarizable cavity surface. In practice, this surface is discretized by finite segments, each with a segment-centered polarizable point charge. The difference between the most common CSMs, the polarizable continum model[41] and the conductor-like screening model[42], is the electrostatic boundary condition at the cavity surface. Within COSMO the electrostatics at the cavity surface are described by a vanishing total electrostatic potential. This condition holds exactly, if the continuum is approximated as a conductor, e.g. a material with an infinit large dieelectric constant $\epsilon{=}\infty$.

The potential steaming from the COSMO surface charges can be interpreted as potential stemming from an average over different solvent configurations. Therefore the COSMO-Lagrangian is also often refered to as free energy of solvation[47,48]

$$\mathcal{L}_{\mathrm{COSMO}} = \langle\Lambda|\hat{H}^{\mathrm{QM}}|\mathrm{CC}\rangle + \frac{1}{2}\sum_{u} Q_u V_u^{QM} \tag{2.18}$$

The last term of equation 2.18 depict the polarization energy, that is defined as energy to creat the cavity surface charges Q_{u} and the interaction between these charges with the total electrostatic potential. The surface charges are polarized by the total QM charg density and are obtained as

$$Q_u = -f(\epsilon)\sum_{\nu}\left[\mathbf{A}^{-1}_{COSMO}\right]_{uv} V_v^{\mathrm{QM}} \ , \tag{2.19}$$

where V_u^{QM} is the potential mediated by the total QM charge distribution at surface segment u. Since the electrostatic boundary condition is valid for ideal conductors only, the obtained surface charges are scaled by an empirical factor

$$f(\epsilon) = \frac{\epsilon - 1}{\epsilon + \frac{1}{2}} \ , \tag{2.20}$$

which accounts for the finite relative permittivity of real solvents. The COSMO response kernel contains the coulomb metric between the segment centers u and v as off-diagonal elements, while the diagonal elements are proportional to the surface area of the respective segment [42]

$$\left[\mathbf{A}_{\mathrm{COSMO}}\right]_{uv} = \begin{cases} (\mathbf{r}_u - \mathbf{r}_v)^{-1} & \text{for } u \neq v \\ 3.8\sqrt{S_u} & \text{for } u = v \end{cases} \tag{2.21}$$

The COSMO electronic coupling operator is given by the contribution due to the coupled-cluster electron density to the polarization energy and is given by

$$\hat{G}_{\mathrm{COSMO}}(\mathbf{D}^{\mathrm{CC}}) = \sum_u \sum_{pq} Q_u V_{u,pq} \hat{E}_{pq} \tag{2.22}$$

2.3 The Ground State COSMO- & PE-CC2 Equations

The ground state wavefunction parameters, are evaluated by requiering that the vector-functions, which are obtained as first partial derivative of the Lagrangian with respect to the lagrange multiplier (Ω_{μ_i}) and cluster amplitudes ($\bar{\Omega}_{\mu_i}$), vanish. For the COSMO- and PE-CC2 scheme in their post-SCF reaction field formulation the vectorfunctions are given by: [36,48]

$$\begin{aligned} \Omega_{\mu_1} &= \frac{\partial \mathcal{L}}{\partial \bar{t}_{\mu_1}} \\ &= \langle \mu_1 | \tilde{W} + \tilde{G}^{\Delta}(\mathbf{D}^{\Delta}_{\mathrm{CIS}}) + [\hat{F}^{\mathrm{emb}}, \hat{T}_1] + [\tilde{W}, \hat{T}_2] | \mathrm{HF} \rangle, \end{aligned} \tag{2.23}$$

$$\begin{aligned} \Omega_{\mu_2} &= \frac{\partial \mathcal{L}}{\partial \bar{t}_{\mu_2}} \\ &= \langle \mu_2 | \tilde{W} + [\hat{F}^{\mathrm{emb}} + \hat{T}_2] | \mathrm{HF} \rangle, \end{aligned} \tag{2.24}$$

$$\begin{aligned} \bar{\Omega}_{\mu_1} &= \frac{\partial \mathcal{L}}{\partial t_{\mu_1}} \\ &= \langle \mathrm{HF} | [\tilde{W} + \tilde{G}^{\Delta}(\mathbf{D}^{\Delta}_{\mathrm{CIS}}), \hat{\tau}_{\mu_1}] | \mathrm{HF} \rangle \\ &+ \sum_{\nu_1} \bar{t}_{\nu_1} \langle \nu_1 | [\hat{F}^{\mathrm{emb}} + \tilde{W} + \tilde{G}^{\Delta}(\mathbf{D}^{\Delta}_{\mathrm{CIS}}), \hat{\tau}_{\mu_1}] + [[\tilde{W}, \hat{\tau}_{\mu_1}], \hat{T}_2] | \mathrm{HF} \rangle \\ &+ \sum_{\nu_2} \bar{t}_{\nu_2} \langle \nu_2 | [\tilde{W}, \hat{\tau}_{\mu_1}] | \mathrm{HF} \rangle, \end{aligned} \tag{2.25}$$

$$\begin{aligned}\bar{\Omega}_{\mu_2} &= \frac{\partial \mathcal{L}}{\partial t_{\mu_2}} \\ &= \langle \mathrm{HF}|[\tilde{W}, \hat{\tau}_{\mu_2}]|\mathrm{HF}\rangle \\ &+ \sum_{\nu_1} \bar{t}_{\nu_1} \langle \nu_1|[\tilde{W}, \hat{\tau}_{\mu_2}]|\mathrm{HF}\rangle \\ &+ \sum_{\nu_2} \bar{t}_{\nu_2} \langle \nu_2|[\tilde{W}, \hat{\tau}_{\mu_2}]|\mathrm{HF}\rangle,\end{aligned} \tag{2.26}$$

The COSMO- and PE-CC2 vectorfunctions are obtained by the general COSMO- and PE-Lagrangian of equation 2.18 and 2.10, in which the cluster operator (equation 2.3) is truncated after double excitations and the doubles cluster equations,

$$\langle \mu_2|\tilde{H} + [\tilde{H}, \hat{T}_2] + \frac{1}{2}[[\tilde{H}, \hat{T}_2], \hat{T}_2]|\mathrm{HF}\rangle \rightarrow \langle \mu_2|\tilde{W} + [\hat{F}, \hat{T}_2]|\mathrm{HF}\rangle, \tag{2.27}$$

are replaced by terms that are correct through first order in the fluctuation potential[10], where the partitioning $\hat{H} = \hat{F} + \hat{W}$ was used, that splits the Hamilton operator $\hat{H}$ into the Fock operator $\hat{F}$ and the flutuation potential $\hat{W}$.[51] Furthermore, a T_1-transformation of the operators $\tilde{O} = \exp(-\hat{T}_1)\hat{O}\exp(\hat{T}_1)$ was performed, in the notation of equations 2.23 to 2.27. For the COSMO- and PE-CC2 scheme in their post-SCF reaction field formulation the vectrofunctions are similar. However, it should be noted again, that COSMO environment is constructed by polarizable point charges[42], while the PE environment contains polarizable dipole moments[36], i.e. the coupling operators are defined differently.

Most importantly for the following discussion are the terms, that contain contributions of the solute/solvent coupling. Within the post-SCF reaction field[36,48], the mutual solute/solvent polarization is split in uncorrelated HF- and correlated CC-contributions, respectively. The uncorrelated contributions are captured by self-consistent COSMO-HF and PE-HF calculations, i.e. the MOs are optimized in the field of polarizable (and static) MM sites, which are in turn self-consistently generated by the HF-electronic charge density. This is taken into account by introducing the embedded Fock operator $\hat{F}^{\mathrm{emb}}$, which includes the environment coupling operator depending on the Hartree-Fock density $\hat{F}^{\mathrm{emb}} = \hat{F} + \hat{G}(\mathbf{D}^{\mathrm{HF}})$.

The correlation contribution to the solute/solvent interaction is included in the operator $\tilde{G}^{\Delta}(\mathbf{D}^{\Delta}_{\mathrm{CIS}})$, which is obtained by subtracting the Hartree-Fock contributions from all operators $\hat{G}$ is build from. Within the post-SCF approach, contributions from this coupling operator occur only in the single excitation parts of the Ω and $\bar{\Omega}$ terms. This is due the fact, that the normal ordered operator $\tilde{G}^{\Delta}(\mathbf{D}^{\Delta}_{\mathrm{CIS}})$ contains only the difference

between the coupled-cluster ground state singles charge density and the COSMO- and PE-Hartree-Fock charge density

$$D^{\Delta}_{pq} = \left(\left\langle \mathrm{HF}\right| + \sum_{\mu_1} \bar{t}_1 \left\langle \mu_1 \right|\right) \exp(-\hat{T}_1)\hat{E}_{pq}\exp(\hat{T}_1)\left|\mathrm{HF}\right\rangle - \left\langle \mathrm{HF}\right|\hat{E}_{pq}\left|\mathrm{HF}\right\rangle \,, \tag{2.28}$$

respectively, i.e. the doubles part was neglected in the difference density construction, such as a $[\tilde{G}^{\Delta}, \hat{T}_2]$ commutator, which would appear in the singles and doubles parts of the vectorfunctions. This post-SCF scheme was motived by two facts[36]: First, the efficiency of the RI-CC2[55] and PE-RI-CC2[36] implementations are founded in the fact that the doubles amplitudes are computed "on the fly" when needed and are thus not saved on disk. Additional like the $[\tilde{G}^{\Delta}, \hat{T}_2]$ term would increase the computational cost. Most importantly, it was argued[36,48] that including doubles amplitudes in the density construction would lead to terms which contain products of these first-order doubles amplitudes. Since the CC2 scheme treats the t_{μ_2} as first order, all terms higher in order, such as products of t_{μ_2} should be neglected. In the following the $\mathbf{D}^{\Delta}_{\mathrm{CIS}}$ term is abbreviated as $\mathbf{D}^{\Delta}$ for simplicity reasons.

2.4 The COSMO & PE-CC2 Jacobi Matrix

In contrast to the state specific approach to excitation energies, in which the Schrödinger equation is solved for each state, within linear response theory excitation energies are obtained by determining the eigenvalues of the Jacobi matrix,

$$\mathbf{A}\vec{\mathrm{R}} = \omega\vec{\mathrm{R}}, \tag{2.29}$$

without explicitly calculating the excited state wavefunctions. The eigenvectors $\vec{\mathrm{R}}$ of $\mathbf{A}$ contain the excited state cluster amplitudes and ω is the corresponding excitation energy. Similar to the ground state cluster amplitudes, $\vec{\mathrm{R}}$ is build of singles (R_{μ_1}) and doubles (R_{μ_2}) excited state amplitudes, in the case of the CC2 Jacobi matrix. The Jacobi matrix $\mathbf{A}$ is defined as the second partial derivative of the Lagrangian with respect to the Lagrange multiplier and cluster amplitudes

$$\mathbf{A}_{\mu\nu} = \frac{\partial^2 \mathcal{L}}{\partial \bar{t}_{\mu} \partial t_{\nu}} \,. \tag{2.30}$$

Depending on the approximation used in the construction of the Jacoby matrix, $\mathbf{A}$ can be non-hermitian and thus the left and right eigenvectors are not equal, like in the case of the CC2 Jacobi matrix.[10] However, the eigenvalues of a particular state are equal for

both eigenvectors. According to ref.[36,48] the COSMO- and PE-CC2 Jacoby matrix for the post-SCF approach is given by

$$A_{\mu_1\nu_1} = \langle\mu_1|[\hat{F}^{emb} + \tilde{W}^{QM} + \tilde{G}^{\Delta}(D^{\Delta}), \tau_{\nu_1}] + [[\tilde{W}^{QM}, \tau_{\mu_1}], \hat{T}_2] + \tilde{G}^{\nu_1}|\mathrm{HF}\rangle \tag{2.31}$$

$$A_{\mu_1\nu_2} = \langle\mu_1|[\tilde{W}^{QM}, \tau_{\nu_2}]|\mathrm{HF}\rangle \tag{2.32}$$

$$A_{\mu_2\nu_1} = \langle\mu_2|[\tilde{W}^{QM}, \tau_{\nu_1}]|\mathrm{HF}\rangle \tag{2.33}$$

$$A_{\mu_2\nu_2} = \langle\mu_2|[\hat{F}^{emb}, \tau_{\nu_2}]|\mathrm{HF}\rangle \tag{2.34}$$

Besides the $\tilde{G}^{\Delta}(D^{\Delta})$ operator, which also appear within the grounds state vector functions, the singles-singles block of the Jacobi matirx contain also a term which describes the mutual polarization between the environment and the change of the electronic density upon excitation. The $\tilde{G}^{\nu_1}(D^{\Delta})$ operator is build by the partial derivative of the environment coupling operator $\tilde{G}^{\Delta}(D^{\Delta})$ with respect to the cluster amplitudes t_{μ_1}. By considering the right transformation of equation 2.29, together with the introduction of an new operator $\hat{R} = \sum_{\nu_1} R_{\nu_1}\hat{\tau}_{\nu_1}$, that contains the single excited state amplitudes ($\{R_{\nu_1}\}$) of the eigenvector $\vec{\mathrm{R}}$, the term can be rewritten to[36,48],

$$\sum_{\nu_1} \Big\langle \mu_1 \Big| \hat{G}^{\nu_1} \Big| \mathrm{HF} \Big\rangle R_{\nu_1} = \Big\langle \mu_1 \Big| \hat{G}^{\Delta}(D^{\nu_1}) \Big| \mathrm{HF} \Big\rangle \tag{2.35}$$

After the right transformation the coupling operator depend on an auxiliary density, that contains the information about the nature of the change in the solutes transition density[36,48],

$$D^{\nu_1}_{pq} = \Big(\Big\langle \mathrm{HF} \Big| + \sum_{\mu_1} \bar{t}_1 \Big\langle \mu_1 \Big| \Big) \exp(-\hat{T}_1)[\hat{E}_{pq}, \hat{R}_{\nu_1}]\exp(\hat{T}_1) \Big| \mathrm{HF} \Big\rangle \ , \tag{2.36}$$

$$= \frac{\partial \mathbf{D}^{\Delta}_{pq}}{\partial t_{\nu_i}} R_{\nu_1} \ . \tag{2.37}$$

The contribution of the transition density is only obtained within the linear response approach. In contrast to that, the state-specific approach lead to contributions arising from the density of a particular excited state.[56]

3 Pair Natural Orbitals for the ground and excited state

Quantum chemical methods that exploit the nature, of electron correlation, by the incorporation of pair natural orbitals, use a pair specific virtual space for the evaluation of two-electron integrals that contain virtual molecular orbitals, as they appear in the Ω, $\bar{\Omega}$ and σ^{R} evaluation. Here, the pair specific virtual space is spanned by pair natural orbitals ($\left|\bar{a}_{ij}\right\rangle$) that are defined for a particular pair of occupied MOs ij and are constructed by a linear combination of canonical virtual molecular orbitals ($\left|a\right\rangle$),

$$\left|\bar{a}_{ij}\right\rangle = \sum_{a} d^{ij}_{a\bar{a}_{ij}} \left|a\right\rangle. \tag{3.1}$$

Without any truncation of the expansion in equation 3.1 the whole virtual space would be included in the construction of PNOs. Thus also pairs which do not contribute to the correlation effects would be considered, leading to no computational benefits. A simple control over the truncation of the PNO expansion is given by including only PNOs, whose eigenvalues of the diagonalized pseudo-pair density [31]

$$d^{ij}_{a\bar{a}} D^{ij}_{ab} d^{ij}_{b\bar{b}} = n^{ij}_{\bar{a}} \delta_{\bar{a}\bar{b}} \tag{3.2}$$

are larger than a given threshold ($n^{ij}_{\bar{a}} \geq T_{PNO}$). With this approach, pairs whose PNOs are connected to large natural occupation numbers $n^{ij}_{\bar{a}}$ are significant for the description of correlation effects. Furthermore, it could be shown that using localized occupied molecular orbitals (LMOs), lead to a more compact virtual space, i.e. the correlation effects of significant pairs are described by less PNOs. [57]

For the ground state, the pseudo-pair density and thus the PNOs are obtained by MP2 calculations, which describe the correlation effects to the ground state through second-order. Using canonical molecular orbitals the MP1 wavefunction parameter are given by

$$t^{ij}_{ab} = \frac{(ai|bj)}{\epsilon_a - \epsilon_i + \epsilon_b - \epsilon_j}, \tag{3.3}$$

where the two-electron integrals $(ai|bj)$ are divided by the difference of the orbital energies ϵ_p. Using LMOs for the occupied/occupied Block of the Fock matrix lead to a non-diagonal form of this matrix. However, using the diagonal elements of the non-diagonal Fock matrix can be used to obtain the MP1 double amplitudes in a smilar way as in equation 3.3,

$$t_{ab}^{ij} \approx \frac{(ai|bj)}{\epsilon_a - F_{ii} + \epsilon_b - F_{jj}}. \tag{3.4}$$

The pseudo-pair density can then be constructed with the (approximated) MP1 doubles amplitudes[31],

$$D_{ab}^{ij} = 2(\tilde{t}_{ac}^{ij} t_{bc}^{ij} + \tilde{t}_{ca}^{ij} t_{cb}^{ij}) \tag{3.5}$$

$$\tilde{t}_{ab}^{ij} = 2t_{ab}^{ij} - t_{ba}^{ij} \tag{3.6}$$

Motivated by the ground state PNO construction, which uses the second-order energy correction the HF energy, excited state PNOs can be constructed with the second-order correction to the CIS transition energy ω^{CIS}, which is obtained by the CIS(D) method invented by Head-Gordan.[58] The CIS(D) correction $\omega^{(2)}$ to ω^{CIS} is given by ground and excited state contributions[32,33]

$$\omega^{(2)} = \omega_{\mathrm{gs}}(t_{\mu_2}^{(1)}, R_{\mu_1}^{(0)}) + \omega_{\mathrm{es}}(R_{\mu_1}^{(0)}, R_{\mu_2}^{(1)}). \tag{3.7}$$

The ground state contribiution ω_{gs} is dependend on the MP1 amplitudes $t_{\mu_2}^{(1)}$, such as the eigenvalue of the CIS Jacobi matrix $R_{\mu_1}^{(0)}$. Of particular interest for the excited state PNO construction is thus the excited state contribution to the CIS(D) correlation energy, that consists of pair contributions $\omega_{ij}^{\mathrm{es}}$ to the total excited state correlation energy[32]

$$\omega_{\mathrm{es}} = \sum_{i \leq j} \frac{\omega_{ij}^{\mathrm{es}}}{1 + \delta_{ij}} = \sum_{i \leq j} \frac{1}{1 + \delta_{ij}} \bar{L}_{ab}^{ij} R_{ab}^{ij}. \tag{3.8}$$

Here the two-electron integrals are summarized as $\bar{L}_{ab}^{ij} = 2\bar{K}_{ab}^{ij} - \bar{K}_{ab}^{ij}$. In contrast to the ground state MP1 amplitudes, the first-order excited state double amplitudes depend on the CIS excitation energy and are given within the diagonal approximation by

$$R_{ab}^{ij} \approx \frac{(ai\bar{|}bj)}{\epsilon_a - F_{ii} + \epsilon_b - F_{jj} + \omega^{\mathrm{CIS}}}. \tag{3.9}$$

Furthermore, the two-electron integrals in Equation 3.9 are dependent on the singles excited state amplitudes through

$$\bar{K}_{ab}^{ij} = (ai\bar{|}bj) = P_{ia,jb}(R_{ci}^{(0)}(ac|bj) - R_{ak}^{(0)}(ki|bj)) \tag{3.10}$$

Both the ω^{CIS} and $R^{(0)}_{\mu_1}$ dependency of R^{ij}_{ab}, justify the use of a seperate PNO basis for the excited state, beside the ground state PNO basis. Especially for long-range charge transfer transitions, which have a highly non-local character. Indeed, calculations in which only the ground state PNO basis was used for both ω_{es} and ω_{gs} result in slower convergence of the PNO truncation errors, due to a much worse error compensation between the errors in ω_{es} and in ω_{gs}. Another downside of using only the ground state PNO basis is that the number of pairs scales linearly with the system size for the ground state, while the number of pairs scales linearly with the chromophore size for the excited state. Thus the ground state PNO basis usually tends to be larger than the excited state PNO basis. The CIS(D)-like pseudo-pair density can then be constructed with the excited state doubles amplitudes[32] through

$$D^{ij}_{ab} = 2(\tilde{R}^{ij}_{ac} R^{ij}_{bc} + \tilde{R}^{ij}_{ca} R^{ij}_{cb}) \tag{3.11}$$

$$\tilde{R}^{ij}_{ab} = 2R^{ij}_{ab} - R^{ij}_{ba}. \tag{3.12}$$

In contrast to the ground state PNO generation which is performed once before solving the ground state coupled-cluster equations, PNOs for the excited state have to be regenerated during the eigenvalue and eigenvector determination, according to criteria, which take into account the change in ω and R during the iterative Davidson algorithm. To check if the current excited state PNO basis is still accurate for the current approximation to the eigenvector and eigenvalue the expression[26,27]

$$1 - |R^0_{\mu_1} \cdot R_{\mu_1}| \geq \beta ||\rho|| \tag{3.13}$$

is evaluated. Here $R^0_{\mu_1}$ is the singles start vector, R_{μ_1} is the current singles vector, β is an empirical parameter and $||\rho||$ is residual norm. New excited states PNOs are generated whenever the condition in equation 3.13 is fulfilled.

The above mentioned scheme for the ground and excited state PNO construction can be simply extended to constructed PNOs for the COSMO- and PE-PNO-CC2 method. Here ground state PNOs are constructed based on COSMO- and PE-MP2 calculations within the PTE reaction field, i.e. COSMO- and PE-Hartree-Fock MOs are used within the particular MP2 calculation. Excited state PNOs are generated based on COSMO- and PE-CIS(D) calculations. For that, the Jacobi matrix is similar to the singles-singels block of the COSMO- and PE-PNO-CC2 Jacobi matrix in equation 2.31, with the exception that the ground state singles amplitudes (equation 2.32) are set to zero and the CC2 double amplitudes are replaced by COSMO- and PE-MP2 doubles amplitudes, respectively. Note, that in this case $(\hat{G}^{\Delta}(D^{\Delta}))$ vanishes, and the transition density in equation 2.36 has a simpler form.

4 Implementation

In this chapter, the details of the implementation of COSMO- and PE-PNO-CC2 in their post-SCF reaction field formulations are discussed. The implementation was performed in the pnoccsd[31,59] program of the `TURBOMOLE` program package[52], in which the PNO-CC2[26] approach was already implemented. Furthermore, it should be noted that the contribution to the excitation energies that arise through the transition density (equation 2.36) in the Jacobi (G^{ν_1}) matrix was already implemented for the methods COMSO-PNO-CIS(D) and -ADC(2) in a previous project[1]. This contribution was extended for the CC2 model to be dependent also on the singles cluster amplitudes, such as Lagrange multiplier. Thus, the main task for implementing COSMO- and PE-PNO–CC2 was the solution of the $\bar{t}_\mu$-t_μ-coupled PE- and COSMO-PNO-CC2 ground state equations. As discussed in the previous sections, within the post-SCF reaction field scheme the electronic density of the quantum system that couples to the polarizable environment is independent of the doubles cluster amplitudes and Lagrange multiplier, such as two-electron integrals. In addition, the environmental coupling operator ($\hat{G}^\Delta(D^\Delta)$) arises only in matrix elements with singles replacements. Therefore the construction and inclusion of $\hat{G}^\Delta(D^\Delta)$ is independent of the PNO construction, allowing for the efficient use of program structures already available in the `ricc2`[55] program of `TURBOMOLE`, namely the `cc_peeffop` subroutine which is used to build the $\hat{G}$ matrix elements.[36,48] Furthermore, both approaches can be implemented at once (except for minor details) since already the canonical methods are using the same subroutine `cc_peeffop`. As a general strategy to solve the $\bar{t}_\mu$-t_μ-coupled PE- and COSMO-PNO-CC2 ground state equations, the approach of the canonical COSMO-CC2[48] is followed, that is the treatment of the non-linear equations as one large set of equations with twice as much variables as for the vacuum case. An alternative would be solving these equations for a fixed difference density in $\hat{G}^\Delta(D^\Delta)$ within a micro loop, while the density is changed in a macro loop, as was done in ref[60].

Within the PNO-CC2 implementation[26] the ground state equations are solved in the subroutine `pno_solve_t0`, in which the residual Ω is evaluated in the subroutine `pno_vecfun`. For the solution of the $\bar{t}_\mu$-t_μ-coupled equations a new subroutine (`pnogsresidual`) was introduced in `pno_solve_t0`, which is controlled by the flag *do_tbar*, that is set to "true" in case the solvation models are used. For this case, a schematic scheme for the program

[1] Focal point practicle: Implementation of COSMO-PNO-CIS(D), - CIS(D_{inf}) -ADC(2) and its application to the L_a and L_b Transitions of Adenine

flow in `pno_solve_t0` in shown in Algorithm 1. The algorithm starts by setting the doubles cluster amplitudes equal to the MP1 amplitudes in the PNO basis, which were obtained during the PNO construction. Within `pnogsresidual`, first Ω is computed in `pno_vecfun`, in which `cc_peeffop` is called in order to compute the $\tilde{G}^{\Delta}_{\mathrm{ij}}(D^{\Delta})$, $\tilde{G}^{\Delta}_{\mathrm{ia}}(D^{\Delta})$, $\tilde{G}^{\Delta}_{\mathrm{ai}}(D^{\Delta})$ and $\tilde{G}^{\Delta}_{\mathrm{ab}}(D^{\Delta})$ matrix elements and save them on file. After this $\tilde{G}^{\Delta}_{\mathrm{ai}}(D^{\Delta})$ is added to Ω_{ai}.
In the next step $\bar{\Omega}$ has to be evaluated. According to ref.[36,48] this can be done as

$$\bar{\mathbf{\Omega}} = \bar{\mathbf{t}} \cdot A + \eta. \tag{4.1}$$

In this notation $\bar{\mathbf{\Omega}}$ and $\bar{\mathbf{t}}$ are vectors containing all singles and doubles elements of the vectorfunctions and Lagrange multiplier, respectively. As apparent from equation 4.1, for the $\bar{\Omega}$ evaluation, a left transformation ($\sigma^{\mathrm{L}}(\bar{t}_{\mu})$) has to be performed with the Lagrange multiplier and the Jacobi matrix. This can als be verified by comparing equations 2.25

Algorithm 1 Solution of the COSMO- & PE-CC2-GS Equations (sketch of `pno_solve_t0`)

Start: set $t^{(1)}_{\mu_1} = \bar{t}^{(1)}_{\mu_1} = \bar{t}^{(1)}_{\mu_2} = 0$; $t^{(1)}_{\mu_2}$=$t^{\mathrm{MP2}}_{\mu_2}$, E_0=0
while (i $\leq$ maxiter) **do**
    call `pnogsresidual`
        set $\Omega = \bar{\Omega} = 0$
        call `pno_vecfun` to compute Ω
        call `pno_eim` to compute E_{ij} and E_{ab} Intermediates
        call `pno_lhtr` to compute $\bar{t} \cdot A$ and add the result to $\bar{\Omega}$
        compute η and add the result to $\bar{\Omega}$
    call `pno_calcener` to compute E_i
    compute $\Delta E = E_i - E_{i-1}$
    compute $\|\Omega_{\mu_1} + \Omega_{\mu_2}\| := \sqrt{\Omega^2_{\mu_1} + \Omega^2_{\mu_2}}$
    compute $\|\bar{\Omega}_{\mu_1} + \bar{\Omega}_{\mu_2}\| := \sqrt{\bar{\Omega}^2_{\mu_1} + \bar{\Omega}^2_{\mu_2}}$
    if ($\Delta E < threnr$ and $\|\Omega_{\mu_1} + \Omega_{\mu_2}\| < thromg$ and $\|\bar{\Omega}_{\mu_1} + \bar{\Omega}_{\mu_2}\| < thromg$) **then**
        converged: **Exit loop**
    end if
    call `pno_solve_pt` to compute perturbative update for $t^{(1)}_{\mu}$
    call `pno_solve_pt` to compute perturbative update for $\bar{t}^{(1)}_{\mu}$
    call `pno_diis` to determine $t^{(i+1)}_{\mu}$ by DIIS
    call `pno_diis` to determine $\bar{t}^{(i+1)}_{\mu}$ by DIIS
end while

and 2.26 with the elements of the Jacobi matrix (equations 2.31-2.34). For the $\sigma^{\mathrm{L}}(\bar{t}_\mu)$ step the E_{ji} and E_{ab} intermediates[36]

$$E_{ab} = \hat{F}_{ab} + \tilde{G}^{\Delta}_{ba}(\mathbf{D}^{\Delta}) - \sum_{dkl}(2t^{ad}_{kl} - t^{ad}_{lk})(ld|kb) \ , \tag{4.2}$$

$$E_{ji} = \hat{F}_{ji} + \tilde{G}^{\Delta}_{ij}(\mathbf{D}^{\Delta}) + \sum_{cdk}(2t^{cd}_{ik} - t^{cd}_{ki})(kd|jc) \ , \tag{4.3}$$

are needed, which are evaluated by calling `pno_eim`. Within this subroutine the occupied/occupied and virtual/virtual block of $\tilde{G}^{\Delta}(D^{\Delta})$ is read from file and added to E_{ji} and E_{ab} according to Equations 4.3 and 4.2. After this, the subroutine `pno_lhtr` is called to perform the left transformation. For that, all two electron integrals are expanded in the ground state PNO basis. As the last step the right hand side vector η has to be added to the result of the left transformation. For this the singles part of η_{ai} has to be added to $\bar{\Omega}_{ai}$[36],

$$\eta_{ia} = 2\tilde{F}_{ia} + 2\tilde{G}^{\Delta}_{\mathrm{ia}}(D^{\Delta}). \tag{4.4}$$

For this purpose $\tilde{F}_{ai}$ is read from the file *fhatia*, which was evaluated previously in `fhatia` during the Ω evaluation. Furthermore the doubles part of the right hand side vector[36]

$$\eta^{ij}_{\bar{a}\bar{b}} = 2 \cdot (2 \cdot (\bar{a}_{ij}i|\bar{b}_{ij}j) - (\bar{b}_{ij}i|\bar{a}_{ij}j)), \tag{4.5}$$

which is a linear combination of two-electron integrals in the PNO basis, has to be added to $\bar{\Omega}_{\mu_2}$. The linear combination in equation 4.5 is constructed by the two-electron integrals which are saved in the array *xijab*. These integrals are evaluated in `pno_fterm` during the computation of Ω. The linear combination is then constructed by calling the routine `pno_tcme_vec`.

After the Ω and $\bar{\Omega}$ evaluation, the energy is computed in the subroutine `pno_calcener`. The polarization energy $\mathrm{E_{Pol}}$ can be combined with the singles correlation energy ($\mathrm{E_S}$) and is given according to ref.[36] by

$$E_S + E_{pol} = \sum_{bj}\left(\tilde{F}^{PE}_{jb} + \tilde{G}^{\Delta}_{jb}(\mathbf{D}^{\Delta})\right)t_{bj} - \tfrac{1}{2}\sum_{bj}\bar{t}_{jb}\tilde{G}^{\Delta}_{bj}(\mathbf{D}^{\Delta}). \tag{4.6}$$

Here, the occupied/virtual block of $\tilde{G}^{\Delta}(D^{\Delta})$ is contracted with the singles cluster amplitudes, while the virtual/occupied part of the $\tilde{G}^{\Delta}(D^{\Delta})$ matrix elements are contracted with the singles Lagrange multiplier. In order to check if the calculation is converged, the difference between the curent energy and the energy of the previous iteration is computed and checked if this quantity is below a user defined threshold. Furthermore the norm of

the residuals is evaluated and checked if a given threshold is undermatched. For Ω the norm is defined as[26]

$$\|\Omega_{\mu_1} + \Omega_{\mu_2}\| := \sqrt{\Omega_{\mu_1}^2 + \|\Omega_{\mu_2}\|^2} < threomg. \tag{4.7}$$

Here the norm squared of the doubles part of the resiual is given by[26]

$$\|\Omega_{\mu_2}\|^2 = \sum_{ia<jb} \Omega_{ab}^{ij}[2\Omega_{ab}^{ij} - \Omega_{ba}^{ij}] + 0.5 \sum_{ia} \Omega_{aa}^{ii}\Omega_{aa}^{ii} \tag{4.8}$$

The same quantities are evaluated for $\bar{\Omega}$. If the calculations is not converged, i.e. the above discussed quantities are not below the given thresholds, new cluster amplitudes and Lagrange multiplier have to be generated and the loop has to be pass through again until the convergence criteria are fulfilled. New amplitudes and Lagrange multiplier are generated in a two step procedure. First a perturbative correction to the current wavefunction parameters are generated by

$$\sum_{\nu} \langle \mu | [\hat{F}, \tau_\nu] | \mathrm{HF} \rangle \Delta t_\nu^{(n)} = -\Omega_\mu(t^{(n)}), \tag{4.9}$$

which is based on the Newton's method for non-linear equations.[51,61] In contrast to the canonical CC2 implementation in which canonical MOs are used and the residual has only to be devided by the orbital energy differences[51,55,61], the use of localized MOs makes it necessary to solve a set of linear equations, that are defined by equation 4.9. The solution of the linear equation to generate the perturbative corrections $\Delta t_\mu^{(n)}$ and $\Delta \bar{t}_\mu^{(n)}$ are performed in `pno_solve_pt`. In order to improve the convergence of cluster amplitudes and Lagrange multiplier the direct inversion of iterative subspace[62,63] (DIIS) scheme is used in addition to generate new wavefunction parameters by an interpolation of the previous parameters. This is done for the set of t_μ and $\bar{t}_\mu$ in the subroutine `pno_diis`.

5 Results

5.1 Computational Details

All calculations and implementations were performed with a local development version of `TURBOMOLE`[52] program package. Here, molecular orbitals are generated using the `dscf`[64] program, in which the Hartree-Fock, COSMO-Hartree-Fock and PE-Hartree-Fock schemes are implemented. The `ricc2`[55] program was used to compute transition energies with the canonical implementations of RI-CC2[55], COSMO-CC2[48] and PE-CC2[36], such as to perform structure optimization on the RI-MP2 and COSMO-MP2 level of theory. DFT[11,12] structure optimizations, such as the generation of Kohn-Sham orbitals were performed with the `ridft`[65] module, using the B3-LYP[66,67] functional and DFT-D3[14] dispersion correction combined with the Becke-Johnson damping function.[15]
For all calculations including ground and excited state PNOs the module `pnoccsd`[31,59] and the hybrid OSV-PNO[31,32] scheme to generrate PNOs was used. Within this approach, PNOs are generated based on a pre-PNO basis which is constructed by merging together OSVs. The OSVs are determined iteratively with the Davidson algorithm. Here, only OSVs are taking into account, whose occupation number are larger than the OSV threshold $T_{\mathrm{OSV}} = 0.1 \cdot T_{\mathrm{PNO}}$.[31] Furthermore, only pairs are included in the PNO construction, whose estimation for the MP2 pair energy is larger than $T_{\mathrm{Pair}} = (0.1 \cdot T_{\mathrm{PNO}})^{\frac{3}{2}}$. In addition, a local auxiliary basis is used for the resolution-of-the-identity approximation. Here, the threshold for selecting this basis is also coupled to the PNO threshold: $T_{\mathrm{RI}} = 10^{\frac{7}{12}} \cdot T_{\mathrm{PNO}}^{\frac{1}{2}}$.[31] If not stated otherwise, molecular orbitals were localized by the intrinsic bond orbital scheme.[68] In addition, for all calculations the $1s^2$ and $2s^22s^22p^6$ core electrons have been kept frozen[69] for the first and second row-elements, respectively.

5.2 Accuracy of the Implementation

The current PNO-CC2 implementation[26] controls the ground and excited state OSV and PNO basis size, such as the selection of the significant pairs and the size of the local RI Basis by a single parameter only, namely the PNO threshold.[31,32] In the limit of a vanishing threshold, the complete OSV and PNO basis for each pair would be used and no pair would be discarded, leading to no computational benefit in comparison to the canonical CC2 implementation. Truncating the PNO and OSV basis leads to deviations

of the transition energies with respect to the canonical method. In order to find a suitable size of the before mentioned quantities, a PNO truncation error analysis has to be performed, that is the calculation of molecular properties for different PNO thresholds and the analysis of the deviation of these properties with respect to the canonical method. For excitation energies, the absolute PNO truncation error

$$|\Delta\omega(\mathrm{T_{PNO}})| = |\omega_{\mathrm{PNO}}(\mathrm{T_{PNO}}) - \omega_{\mathrm{Canonical}}|, \tag{5.1}$$

is given by the absolute value of the difference of the excitation energy obtained with the canonical and the PNO implementation by using a certain PNO threshold. In the special case of solvatochromic shifts, which are obtained as the difference of transition energy of a particular state in two different media (for example in solution and in vacuum)

$$\omega_{\mathrm{Shift}} = \omega_{\mathrm{Sol}} - \omega_{\mathrm{Vac}}, \tag{5.2}$$

the PNO truncation errors can cancel out because the absolute PNO truncation error of a particular solvatochromic shift is obtained by the difference of the errors in solution and in vacuum

$$|\Delta\omega_{\mathrm{Shift}}(\mathrm{T_{PNO}})| = |\Delta\omega_{\mathrm{Sol}}(\mathrm{T_{PNO}}) - \Delta\omega_{\mathrm{Vac}}(\mathrm{T_{PNO}})|. \tag{5.3}$$

In the following discussion, the implemented methods PE- and COSMO-PNO-CC2 are analyzed with regard to their convergence of the PNO truncation errors, in particular in comparison to the already existing implementation for the vacuum case (PNO-CC2). In addition, the PNO error compensation for solvatochromic shifts is analyzed, such as the correctness of the implementation, which is tested on small molecules by using a vanishing PNO threshold and comparing the obtained excitation energies to the canonical implementation.

It should be noted, that the following discussion of truncation errors is oriented on the intrinsic methodic error of the CC2 approach, which can be estimated for singulett 0-0 transitions as to be of the magnitude of $\sim 0.2\,\mathrm{eV}$ [70], when considering the mean absolute error presented in the mentioned study. Thus, an appropriate threshold should lead to errors negligible with respect to this methodic error, that is an error of about $\sim 0.01\,\mathrm{eV}$. For the PNO-CC2 approach, it could be shown on the hand of the Schreiber benchmark set [71], that the mean absolute value (MAE) drops below $\sim 0.01\,\mathrm{eV}$ for a threshold of 10^{-7}, while the maximal error fulfills this criteria when using a threshold of at least 10^{-8}.[26] Hence, as a guideline for an appropriate COSMO- and PE-PNO-CC2 threshold these values are taken. For the PNO truncation error analysis, organic dyes were selected whose $n\pi^*$ and $\pi\pi^*$ transitions are significantly shifted in solution. The above mentioned Schreiber test set [71] contains mainly unsubstituted aromatic compounds, such as a significant number

of Rydberg states and is thus rather inappropriate as benchmark test set for solvation effects on transition energies.

Unless stated otherwise, all calculations presented in the following section were performed with structures optimized at the COSMO-RI-MP2/cc-pVTZ[72] and RI-MP2/cc-pVTZ[72] level of theory for the calculation in solution and in vacuum, respectively. For the calculations of excitation energies, the aug-cc-pVTZ[72] basis set was used. For all calculations the corresponding auxiliary basis set were used for the resolution-of-the-identity approximation.[73]

5.2.1 Accuracy of the COSMO-PNO-CC2 Implementation

In the first step, COSMO-PNO-CC2 calculations were performed on the small molecules acrolein, acetone and methylencyclopropene (MCP), which were also the objective of a former analysis on solvation effects by PCM-CCSD calculations.[74] Acrolein and acetone were considered in water (ϵ_r = 80.36, n_D=1.333)[75], while MCP was computed in methanol (ϵ_r = 33.60, n_D=1.328).[75] For acrolein the first $n\pi^*$ and $\pi\pi^*$ transitions, for acetone the first $n\pi^*$ state and for MCP the first $\pi\pi^*$ transition were analyzed. Note that the relative order of the $\pi\pi^*$ state of acrolein is changed in vacuum, based on RI-CC2 calculations, as can be seen in Table 5.1.

The transition energies obtained with the canonical COSMO approach are summarized together with the experimental energies in Table 5.1. Except for the $\pi\pi^*$ transition of acrolein, the computed energies are in good agreement with the corresponding experimental data. Besides effects not captured by the COSMO approach, like possible hydrogen bonding of water molecules with the carbonyl group of acrolein, the author of ref[74] argued that not captured vibronic effects might be the reason for the high deviation of this particular state. Most importantly, COSMO-PNO-CC2 using the whole virtual space for each pair, led to the same transition energies (for the provided five decimal places in the `TURBOMOLE` output), as the canonical COSMO-RI-CC2 implementation, indicating the correctness of the here discussed COSMO-PNO implementation.

Table 5.1: Selected experimental $\omega_{Sol}^{Exp.}$, computed ω_{Sol}^{CC2} transitions energies, such as solvatochromic shifts $\Delta\omega_{Shift}^{CC2}$ of acrolein, acetone and methylencyclopropene (MCP).

Name	Solution	Char.	$\#_{Vac}$	$\#_{Sol}$	$\omega_{Sol}^{Exp.}$ [eV]	ω_{Sol}^{CC2} [eV]	$\Delta\omega_{Shift}^{CC2}$ [eV]
Acrolein	Water	$n\pi^*$	S_1	S_1	3.94[76]	4.00	0.15
		$\pi\pi^*$	S_4	S_2	5.90[77]	6.34	-0.45
Acetone	Water	$n\pi^*$	S_1	S_1	4.49[78]	4.65	0.12
MCP	Methanol	$\pi\pi^*$	S_1	S_1	4.69[79]	4.72	0.22

As shown in Table 5.1 the locally excited transitions of the presented small molecules are significantly shifted, when moving from the vacuum into solution. For example, the $\pi\pi^*$ transition of Acrolein is red-shifted by 0.45 eV in water in comparison to the vacuum case, while the $n\pi^*$ transition is blue-shifted by 0.15 eV. The blue-shift of the $n\pi^*$ transition can be explained, by a favorable stabilization of the lone pairs of the carbonyl group in the ground state with respect to the excited state, in which the charge density stemming from the lone pairs is shifted to the π-system.
The PNO tuncation errors of the solvatochromic shifts, the vacuum transitions energies and the excitation energies computed with the COSMO implementations are visualized in Figure 5.1 a)-d). For these small molecules, a loose PNO truncation range was chosen $(10^{-4} - 10^{-6})$, in order to analyze the region, in which the truncation errors are about of the magnitude of the intrinsic error of the CC2 approach. In contrast to larger molecules, nearly all pairs are significant for the description of the correlation effects of the ground

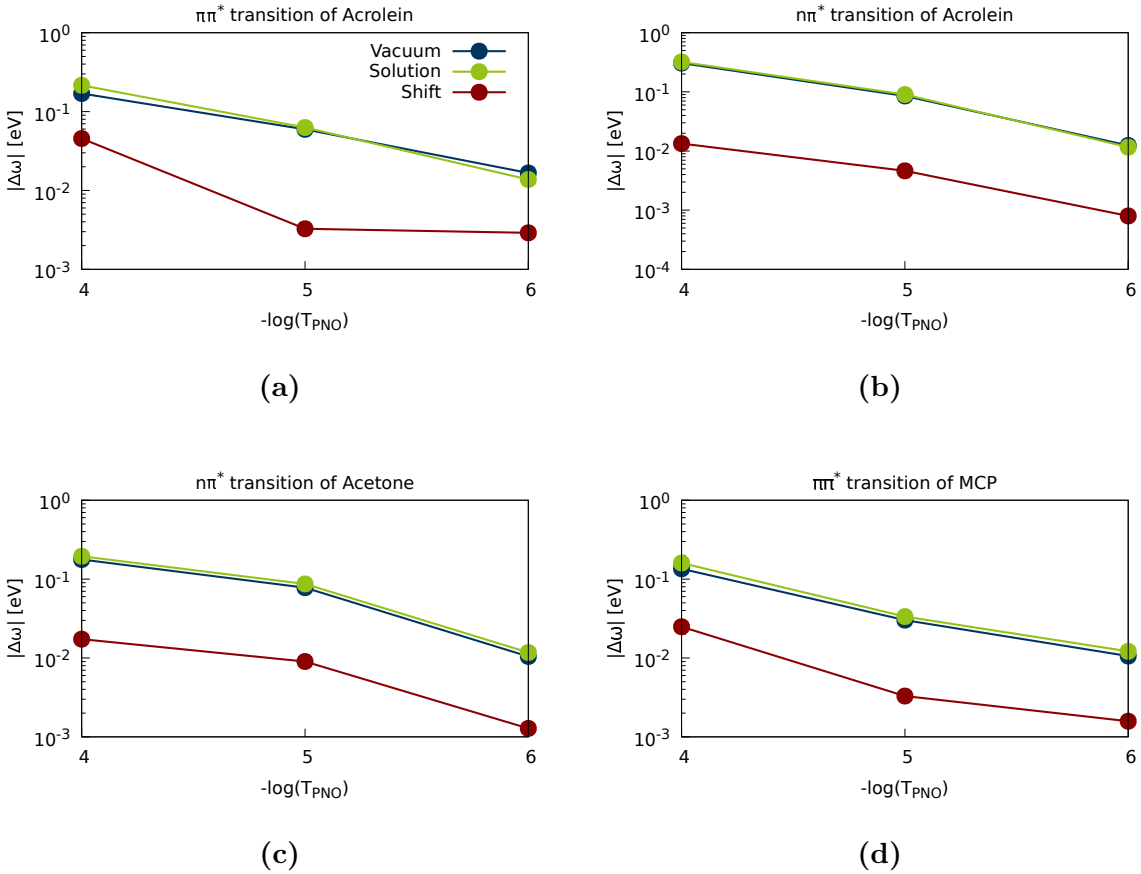


Figure 5.1: PNO truncation error of the vertical excitation energies of the first $\pi\pi^*$ and $n\pi^*$ transitions of Acrolein in water (a) and b) respectively), the first $n\pi^*$ transition of Acetone in Water and the first $\pi\pi^*$ transition of Methylencyclopropene (MCP) in methanol (green lines), such as the corresponding vacuum energies (blue lines) and shifts (red lines). The truncation errors are obtained as the difference of the energies obtained with the canonical COSMO-RI-CC2 method and the COSMO-PNO-CC2 method using the aug-cc-pVTZ basis set.

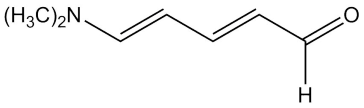
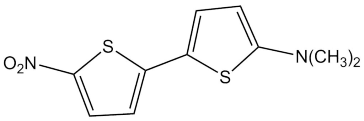
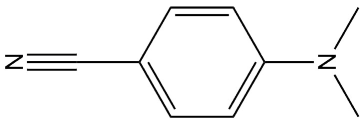
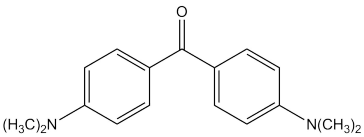
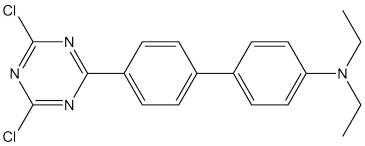
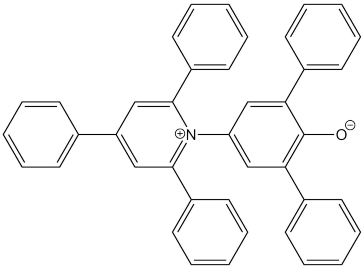
and excited state of acrolein, acetone and MCP. Thus, only very loose PNO thresholds lead to a significant discard of pairs. As a consequence, a PNO threshold of 10^{-4} produces a truncation error in the range of 0.15 eV–0.2 eV for the COSMO and vacuum calculations, while for a threshold of 10^{-6} errors of ~ 0.01 eV were obtained, which are negligible in comparison to the intrinsic error of the CC2 approach. Most importantly, the convergence of the truncation errors obtained by the COSMO-PNO-CC2 approach, is in good agreement with the convergence of the errors obtained by the vacuum PNO-CC2 calculations, as can be seen in Figure 5.1. Therefore a beneficial error compensation for the solvatochromic shifts can be observed, for all presented thresholds. This leads to the tendency, that the truncation errors of the shifts are about one order of magnitude smaller than the corresponding errors for the vacuum and COSMO energies. Thus, already for the loose PNO threshold of 10^{-4}, truncation errors for the shifts were obtained, which are in the range of ~ 0.05 eV (for the $\pi\pi^*$ transition of acrolein (Fig. 5.1 a))) to ~ 0.01 eV (for the transition of $n\pi^*$ transition of acrolein (Figure 5.1 b))).

The above discussed $\pi\pi^*$ and $n\pi^*$ transitions depict locally excited (LE) states. In contrast to that, charge transfer (CT) states involve a long-range transfer of charge density during the transition. For these kinds of transitions, it has been shown, that the diagonal approximation in equation 3.9 used for the generation of excited state PNOs, which neglects the off-diagonal elements of the Fock matrix, lead to a slower convergence of the truncation errors in comparison to LE transitions.[26,33] The origin of this tendency is that these kind of transitions are described by pairs which have a small significant number of PNOs.[26,33] Consequently, these PNOs tend to be inflexible towards approximations and the diagonal approximation has to be replaced by a Laplace transformation of the denominator, that contains the Fock matrix elements.[26,33]

In order to investigate, if CT processes can be described with the same convergence tendency by the COSMO-PNO-CC2 method, as for the vacuum PNO-CC2 approach, the charge transfer transitions of six organic molecules are investigated. Five of these molecules have the typical push-pull structure, in which a donor goup is seperated by an aromatic system from the acceptor group. These molecules are: (2E,4E)-5-(di-methylamino)-2,4-pentadienal (pentadienal) in water[80], 5-(di-methylamino)-5'-nitro-2,2'-bisthiophene (bisthiophene) in water[81], 4-dimethylaminobenzonitrile (DMBAN) in acetonitrile[48], 4,4'-Bis(N,N-dimethylamino)benzophenone (Michler's ketone) in formamide[82] ($\epsilon_r = 111.0$, n_D=1.446)[75] and 4-dichloro-6-[p-(N,N-diethylamino)biphenylyl]-1,3,5-triazine (DBQ) in dimethylsulfoxide (DMSO)[83] ($\epsilon_r = 1.479$, n_D=46.71)[]. In contrast to that the CT process of 2,6-Diphenyl-4-(2,4,6-triphenylpyridin-1-ium-1-yl)phenolate (B30) (computed in water) occur between the phenolate moiety and the pyridinium ring of this dye. Except for DMBAN (S_2) all considered transitions are S_1 states in solution. The corresponding NTOs are summarized in the appendix (see Table 7.2).

The structural formulas of these compounds are depicted in Table 5.2, together with excitation energies and shifts based on the canonical RI-CC2 and COSMO-RI-CC2 calculations. For DBQ the structure provided in ref.[84] was used for both, COSMO-CC2 and the corresponding vacuum calculations. As a start structure for the structure optimization of DMABN the structure provided in ref[48] was used. The vacuum and COSMO structure for the B30 dye was taken from ref[85], such as the vertical excitation energies presented in Table 5.2. It should be noted that all PNO calculations for this dye were performed with the aug-cc-pVDZ[72] basis set.
As summarized in Table 5.2, the charge transfer leads to a relative large red-shift for all presented molecules. This tendency is typical for push-pull systems, in which a charge transfer occur from a donor to an acceptor group and can be explained by an increase of

Table 5.2: Structural formula of pentadienal, bisthiophene, DMBAN, Michler's ketone, DBQ and B30. Vacuum excitation energies, shifts, such as energies in solution are given in eV. All energies are obtained by COSMO-RI-CC2 and RI-CC2 calculations. For further informations please see text.

Name	Molecule	Solvent	$\omega_{\text{Vac}}^{\text{CC2}}$	$\omega_{\text{Sol}}^{\text{CC2}}$	$\omega_{\text{Shift}}^{\text{CC2}}$
Pentadienal		water	4.23	3.60	-0.63
Bisthiophene		water	3.11	2.54	-0.56
DMABN		acetonitrile	4.67	4.34	-0.33
Michler's ketone		formamide	4.13	3.61	-0.51
DBQ		DMSO	3.07	2.69	-0.38
B30		water	1.22[85]	1.88[85]	-0.66

the dipole moment upon excitation, which lead to a favorable stabilization of the excited state with respect to the ground state.[86]

For DMBAN, bisthiophene, pentadienal and Michler's Ketone, the PNO truncation errors of the CT states are presented in the range of 10^{-6}–10^{-8} in Figure 5.2 a)-d). Except for the pentadienal molecule, truncation errors of the magnitude of the intrinsic error of the CC2 method were obtained for a threshold of 10^{-6} for COSMO and vacuum energies. For this threshold, the errors obtained for Michler's Ketone are very similar for both the vacuum (0.26 eV) and COSMO (0.27 eV) calculations, leading to a beneficial error compensation for the shift (0.01 eV). In contrast to that, the errors for DMBAN, bisthiophene tend to be in the region of ~ 0.1 eV, while the errors for the shifts are roughly one magnitude smaller.

Lowering the threshold to a value of 10^{-7}, lead in the case of pentadienal to a lowering of the vacuum PNO truncation error to a value of $\sim 10^{-4}$ eV (see Figure 5.2 b)), which is two magnitudes smaller than the corresponding value obtained by the COSMO approach

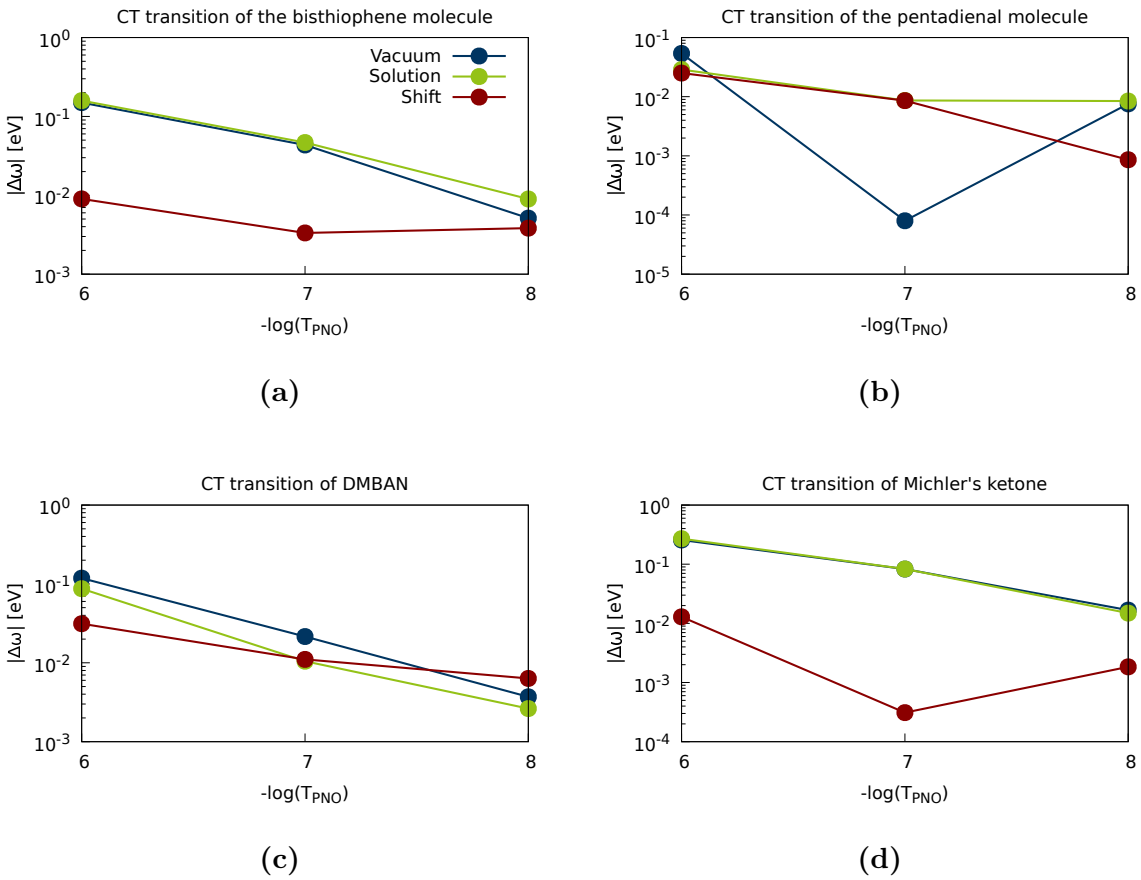


Figure 5.2: PNO trucation error of the vertical excitation energies and solvatochromic shifts of: a) 5-(di-methylamino)-5'-nitro-2,2'-bisthiophene (bisthiophene), b) (2E,4E)-5-(di-methylamino)-2,4-pentadienal (pentadienal) c) DMBAN and d) Michler's ketone. The blue lines denote the vacuum, the green lines denote the COSMO and the red lines denote shift truncation errors, respectively. For further informations please see text.

($\sim 10^{-2}$ eV). For a threshold of 10^{-8} the error for the vacuum energy rise again to a value of ($\sim 10^{-2}$ eV) and is close to the corresponding error of the COSMO energy. The reason for the extraordinary small truncation error for a threshold of 10^{-7} is a fortunate error compensation of the ground and excited state correlation contributions described by the corresponding PNO basis. [27,33]

For a threshold of 10^{-8}, the errors of the COSMO and vacuum energies are one magnitude below the intrinsic error of the CC2 method, while the largest error was obtained for Michler's Ketone for the vacuum case and amounts to 0.016 74 eV. The convergence of the truncation errors described by the COSMO and vacuum calculations are of the same tendency for the described organic molecules. However, for B30 and DBQ a different convergence tendency was obtained. The truncation errors for these molecules are depicted in Figure 5.3.

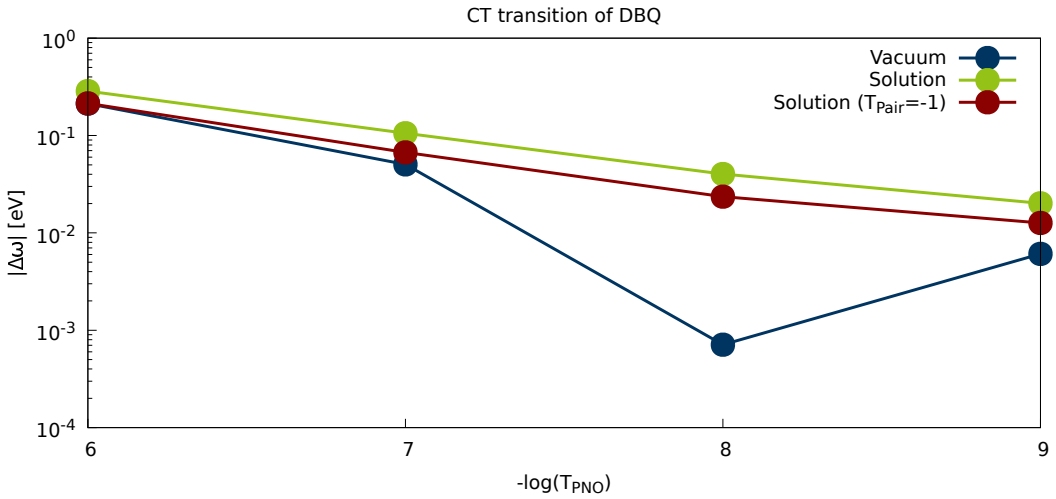
The truncation errors of the first transition of DBQ are presented in Figure 5.3 a). For this transition the COSMO transition energies show a slower convergence than the corresponding vacuum energies. For a threshold of 10^{-7}, for example, an error of ~ 0.11 eV was obtained, in comparison to an error of ~ 0.05 eV. For the lower threshold of 10^{-8} and 10^{-9} the error still do not drop below 0.01 eV and amouts to ~ 0.04 eV and ~ 0.02 eV, respectively. In comparison to that, the truncation errors of the corresponding PNO-CC2 calculations are below 0.01 eV.

The same tendency was observed for B30, where the truncation errors are even higher: ~ 0.15 eV for a threshold of 10^{-7} and ~ 0.07 eV for a threshold of 10^{-8}. A comparison with the corresponding vacuum errors was not possible for this dye since the vacuum energies converge even slower. Here, the error amounts to ~ 0.13 eV even for a threshold of 10^{-9}.

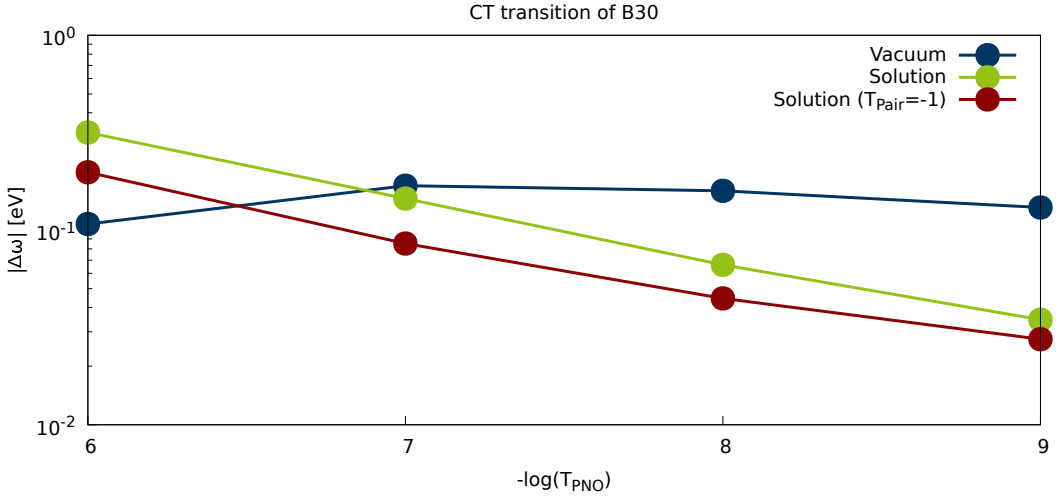
In order to exclude possible effects connected with the local RI approximation and pair discard, vacuum calculations were performed in which the discard of pairs and the local RI basis were switched off. For these calculations, nearly the same truncation errors were obtained as for the calculation, in which these approximations were considered.

A possible reason for the slower convergence of the vacuum transition energies is that the ground state wavefunction of B30 contains a sizeable correlation contribution from single excitations [85] which can not be captured by the MP1 wavefunction the PNOs are constructed from. Therefore the transition energies are red-shifted, since the ground state is higher in energy due to the neglection of the correlation contributions of the singels excitations. However, the excitation energies in solution show a faster convergence. Here it can be argued that the single excitations of the ground state also describe the important contribution to the S_1 state, i.e. the ground state singles cluster amplitudes are similar to the excited state singles amplitudes. [85] These singles amplitudes counteract the polarity of the ground state, which is caused by the large charge separation of the betaine structure. Since in polar solvents polar states are favored, it might be possible that the contribution

of the singles amplitudes are reduced and thus the truncation errors converge faster in solution than in the vacuum case.
The COSMO calculations on the excitation energies of B30 and DBQ include already the Laplace transformation. Here for B30 270 Laplace pairs were considered, which is roughly 12 % of all pairs taken into account. Thus a further investigation on the dependence of the truncation errors with respect to the neglection of pairs were performed. Therefore calculations were performed, in which no pair was discarded because of too small energy



(a)



(b)

Figure 5.3: PNO truncation error of the vertical excitation energies and solvatochromic shifts of: a) DBQ and b) B30. The blue lines denote the vacuum and the green lines denote the COSMO truncation errors, respectively. COSMO truncation errors obtained with a threshold of T_{Pair}=-1 are presented by the red lines. For further informations please see text.

contributions, by setting the pair energy threshold (T_{Pair}) to a negative value. Thus only pairs are neglected, whose PNO basis is vanishing at the corresponding PNO threshold. The results are depicted in Figure 5.3 with a red line. In the case of a threshold of 10^{-7}, the truncation error was reduced by including these pairs by roughly 40 % for DBQ and B30, respectively. The same tendency was observed for the other thresholds. As can be seen in Figure 5.3 a) the truncation error of the CT state of DBQ converges slower in solution in comparison to the vacuum. This can be rationalized by the fact that the polar solvent DMSO enhances the charge transfer upon excitation as can be assured by the dipole moments of the excited states, which amount to 28.6 D and 37.0 D in vacuum and DMSO, respectively. The dipole moments were computed at the ADC(2) and COSMO-ADC(2) scheme using the aug-cc-pVTZ[72] basis set, respectively. Based on these results, the energy threshold for the selection of the significant ground and excited state pairs (T_{Pair}), that are coupled to the PNO threshold and was set to a vanishing value in the above calculations, is not properly adjusted. Thus, further work will be devoted to adjust and test the coupling between the different thresholds on the example of the first transition of B30 and DBQ for the COSMO-PNO-CC2 method.

5.2.2 Accurancy of the PE-PNO-CC2 implementation

The current PE-PNO-CC2 implementation was tested on two systems. The first system is acrolein solvated in acetonitrile. Here, solely the acrolein molecule is treated as the QM systems, while the potential of twenty-nine acetonitrile molecules are represented by 174 static MM sites, including multipoles up to quadrupole moments, such as 174 polarizable dipole moments. The second system is diminazene embedded in an environment of nine water molecules and two adenosinmonophosphat derivatives, such as two thymidinemonophosphat derivatives. Here the diminazene is considered in its doubly protonated form, where the protonations are performed on the amidine group (see Figure 5.4 a) for the chemical formula). For this system, the polarizable MM part is built by 181 static multipoles (up to quadrupole moments) and polarizable dipoles. Both systems together with their MM potentials were kindly provided by the author of ref.[39].

The current PE-PNO-CC2 implementation does not contain the possibility to include effective core potentials for the MM Sites, which are needed to counteract an artificial charge transfer from the QM subsystem to the MM subsystem, which was observed by using augmented basis functions in a former study.[39] Therefore, the cc-pVTZ[72] basis set together with the Pipek-Mezey[87] localization scheme was used, since this localization method give the lowest truncation errors for basis functions without diffuse functions.[32,33] Vacuum excitation energies were obtained by using the same chromophore structures as for the PE calculations.

In case of the acrolein system, the first $n\pi^*$ and $\pi\pi^*$ transitions were considered, while

for the diminazene the first $\pi\pi^*$ transition was examined. Based on the CC2 and PE-CC2 calculations the $n\pi^*$ transition of acrolein is blue-shifted by 0.25 eV, while the $\pi\pi^*$ transition is red-shift by 0.28 eV. For the first transition of diminazene a red-shift of 0.14 eV was obtained. As for the COSMO-PNO appraoch, also for the PE-PNO scheme the correctness of the implementation was checked by using the whole virtual space for each pair, taking into account all pairs and switching off the local RI approximation. This was done for the mentioned transitions of acrolein embedded in acetonitrile with the result that the energies are equivalent with respect to the five decimal places provided in the TURBOMOLE output.

In Figure the obtained truncation errors are depicted. For both transitions of acrolein a truncation error of more than 0.2 eV were obtained for $T_{PNO}=10^{-4}$ in the case of the isolated and solvated molecule, while a beneficial error compensation leads to errors of the shifts that at least one order of magnitude lower than the intrinsic error of CC2. The transition energies reach this accuracy for a threshold of $T_{PNO}=10^{-6}$.

Besides the smaller thresholds used, that account for the size of the diminazene molecule,

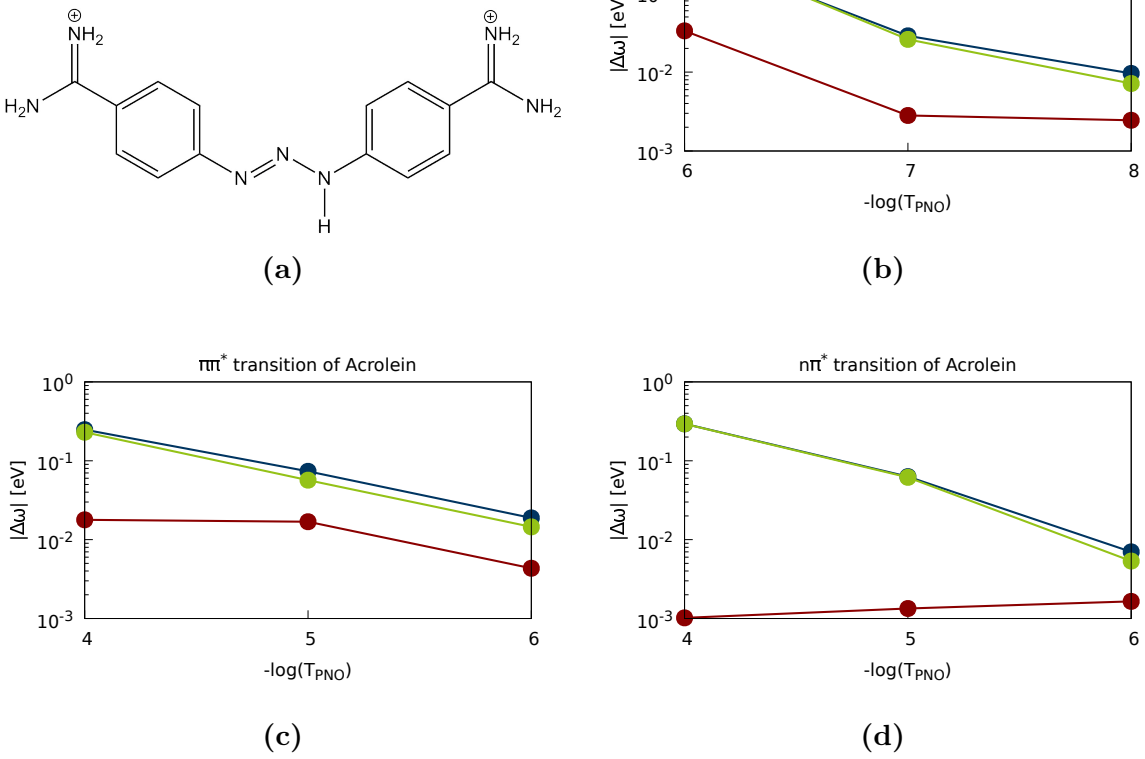


Figure 5.4: a) Chemical formula of Diminazene. Truncation errors of the first $\pi\pi^*$ transition of Diminazene b), the first $\pi\pi^*$ (c)) and $n\pi^*$ (d)) of acrolein obtained by PE-PNO-CC2 and PE-RI-CC2 using the cc-pVTZ basis set. For further informations please see text.

the same tendencies can be observed for the first transition of diminazene. For a higher threshold ($T_{PNO}=10^{-6}$) errors larger than 0.35 eV were obtained. Due to the similar convergence of the errors for the vacuum and solution excitation energies, the error for the shift only amount to 0.03 eV for $T_{PNO}=10^{-6}$. Errors negligible with respect to the methodic error are obtained for $T_{PNO}=10^{-7}$ (~ 0.03 eV) and $T_{PNO}=10^{-8}$ (~ 0.01 eV).

5.3 Performance of the COSMO-PNO-CC2 Implementation

In this section, the performance of the COSMO-PNO-CC2 implementation is investigated and compared to the canonical $\mathcal{N}^5$-scaling COSMO-RI-CC2 implementation. Therefore the computational costs in terms of total wall time of the most elaborate mathematical transformation during the calculation of transition energies within linear response theory were determined for both implementations. For the solution of the ground state coupled-cluster equations, the computation of the vector functions for the cluster amplitudes (Ω) and Lagrange multiplier ($\bar{\Omega}$) are the most time-consuming steps. Since the determination of the vector function $\bar{\Omega}$ can be split in the left-hand transformation of the Lagrange multiplier with the Jacobi matrix σ^L and the addition of the right-hand side vectors η to σ^L, and the computational costs for the $\bar{\Omega}$ evaluation are dominated by σ^L, only the left-hand side is considered in the following. For the evaluation of vertical excitation energies, the eigenvalues of the Jacobi matrix have to be determined. Here, the most expansive step is the right-hand transformation of the Jacobi matrix with a trial vector within the Davidson procedure.

For the three above mentioned transformations, the time scaling with respect to the system size $\mathcal{N}$ was determined by considering the first transition of zwitter-ionic Glycinechains. For the system size, the canonical choice was chosen, namely the total number of AO basis functions. However, a different choice, for example, the number of atoms of the considered molecule can also be used, leading to a different pre-factor exponent c of the general power-law[31]

$$t(\mathcal{N}) = 10^c \cdot \mathcal{N}^B, \tag{5.4}$$

while the scaling exponent B would be the same for both cases. A systematical enlargement of the system size was achieved by considering a continuously duplicated aminoacid-polymer ($(Gly)_{2^k}$ with $k = 0, 1, 2, 3, 4, 5, 6$). For all calculations, the aug-cc-pVDZ[72] basis set was used. The structures of the peptide was taken from ref[33]. The smallest system, that is a single Glycine molecule, consists of 160 AO basis functions and 10 atoms, while the largest molecule is build of 64 Glycine units and includes 7657 AO basis functions and 451 atoms. In these calculations, COSMO surface charges are taken to approximate

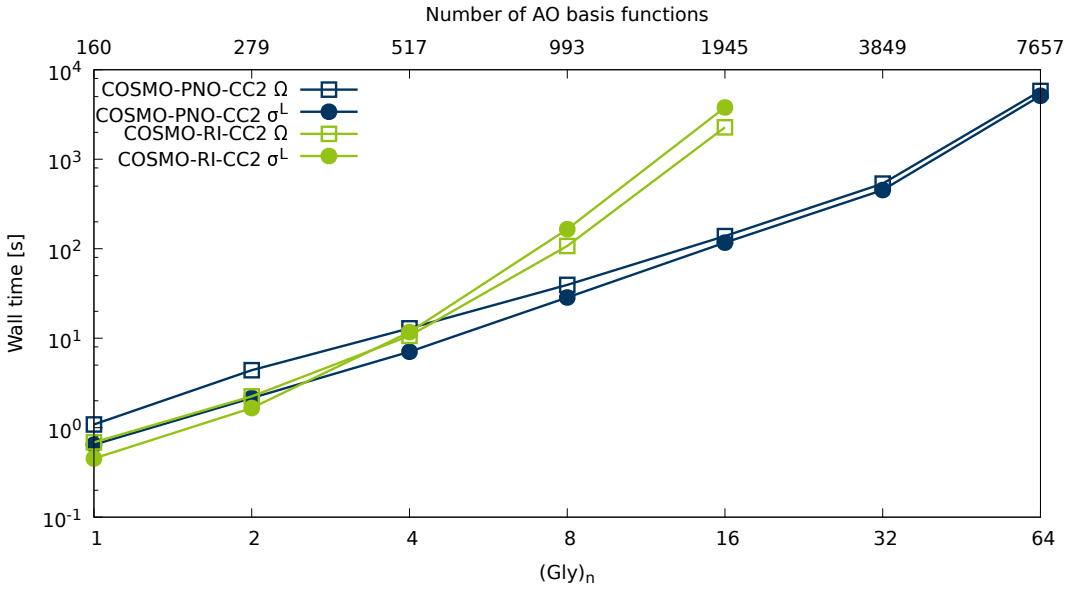
the response of water as the solvent, e.g. a dielectric constant and a refractive index of ϵ=86.30 and n_D=1.333[75] was used, respectively. A PNO threshold of $T_{PNO}=10^{-8}$ for the COSMO-PNO-CC2 calculations was choosen. The thread-parallel calculations were performed on a machine with 20 Intel Xeon Gold 6230 CPUs. The total wall times of Ω, σ^L and σ^R for each system size were obtained by averaging over three consecutive evaluations of these quantities during the iterative schemes in which these transformations were performed. For the evaluation of the total scaling, equation 5.4 was fitted to three data points obtained for the largest molecular systems, i.e. for the PNO approach Gly_{16}, Gly_{32} and Gly_{64} were chosen. Due to the high computational cost of the $\mathcal{N}^5$ canonical COSMO-RI-CC2 implementation, calculations with the $(Gly)_{32}$ were not performed anymore. Thus for the canonical implementations equation 5.4 was fitted to the data obtained by the calculations of Gly_4, Gly_8 and Gly_{16}.
The time-scalings obtained by fitting equation 5.4 to the total wall time needed for the evaluation of Ω, σ^L and σ^R with respect to the number of AO functions are summarized in Tabel 5.3, while the computed timings with respect to the size of the system are depicted in 5.5. As can be seen in 5.5 a), the evaluation of the vector function is slightly more expansive for the PNO implementation than for the canonical implementation, for the smaller Glycinechains ($(Gly)_{1\text{-}4}$). The same tendency holds for the Jacobi left and right (5.5 b)) transformation, when considering the systems $(Gly)_{1\text{-}2}$. The reason for that is a higher overhead for the integral evaluation, which is significant for systems for which only a small fraction of pairs are discarded. However, the PNO-implementation needs significantly less computational time for the evaluation of Ω, σ^L and σ^R in case of the larger chains. The computation of Ω for $(Gly)_{16}$, for example, takes $\sim 138\,s$ with the PNO-implementation, while $\sim 2274\,s$ were needed with the canonical code. Based on the presented data, the scaling of the evaluation of one vector function is reduced for the canonical COSMO implementation to $\mathcal{O}(\mathcal{N}^{2.73})$ for the current COSMO-PNO scheme. Same holds for the left-hand and right-hand transformations. The time complexity of these transformations is reduced by the PNO implementation to $\mathcal{O}(\mathcal{N}^{2.73})$ for the left transformation and to $\mathcal{O}(\mathcal{N}^{2.50})$. Using the power-law for the evaluation of Ω, the time needed to compute this transformation is estimated to $\sim 537\,500\,s$ ($\sim 6.25\,d$) for the

Table 5.3: Time scaling of the most time consuming transformations (Ω, σ^L and σ^R) during the computation of vertical excitation energies using the canonical COSMO-RI-CC2 and the COSMO-PNO-CC2 approach. As system size the total number of AO basis functions $\mathcal{N}_{bf}$ was used within the calculation of the first excitation of Glycinechains (Gly_n) using the aug-cc-pVDZ basis set.

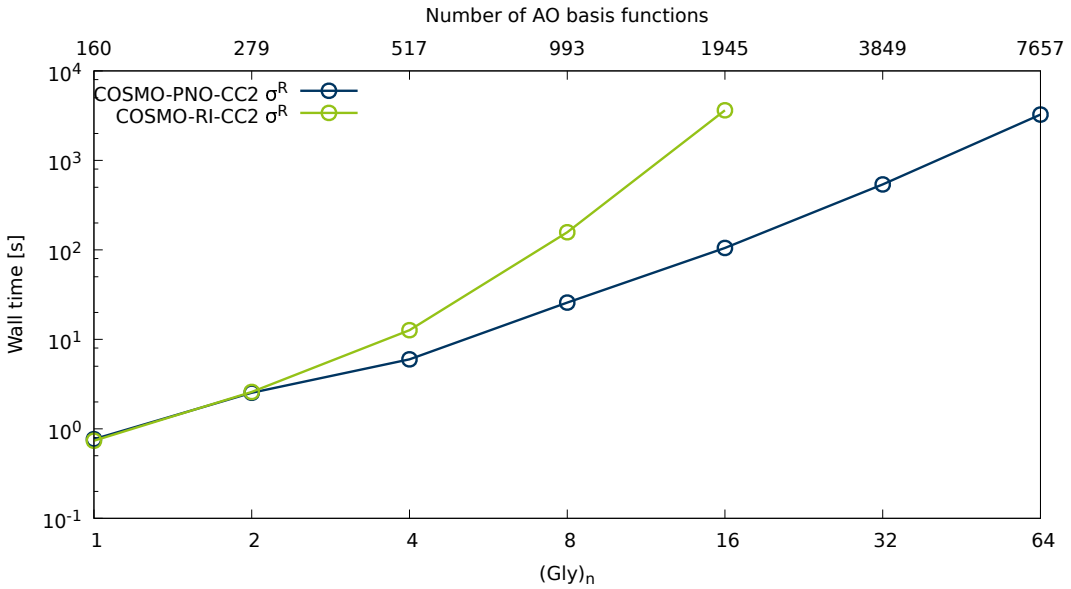
Method	t_Ω	t_{σ^L}	t_{σ^R}
COSMO-RI-CC2	$10^{-10.0}\cdot\mathcal{N}_{bf}^{4.05}$	$10^{-10.8}\cdot\mathcal{N}_{bf}^{4.36}$	$10^{-10.8}\cdot\mathcal{N}_{bf}^{4.27}$
COMSO-PNO-CC2	$10^{-6.9}\cdot\mathcal{N}_{bf}^{2.73}$	$10^{-7.1}\cdot\mathcal{N}_{bf}^{2.76}$	$10^{-6.2}\cdot\mathcal{N}_{bf}^{2.50}$

COSMO-RI-CC2 method, while for the PNO implementation $\sim 5800\,\mathrm{s}$ ($\sim 1.6\,\mathrm{h}$) were needed.

Having in mind, that on the one hand mostly 10-20 iterations are performed until convergence of the ground state equations and that on the other hand also the left hand-



(a)



(b)

Figure 5.5: Averaged total wall time for the evaluation of the most elaborate steps during the COSMO-PNO-CC2 and COSMO-RI-CC2 calculations. The wall time of the evaluation of the vectorfunction (Ω) and the left-transformation of the Lagrange multiplier with the Jacobi matrix (σ^L) are shown in a), while the costs for the right-transformation is shown in b). The averaging were carried out for three concecutive iterations of Ω and σ^L, respectively.

transformation has to be performed for the solution of the COSMO-coupled-cluster ground state equations, this example impressively shows that the COSMO-PNO approach enables the computation of solvent effects on excitation energies of large molecular systems in the framework of COSMO coupled-cluster theory.

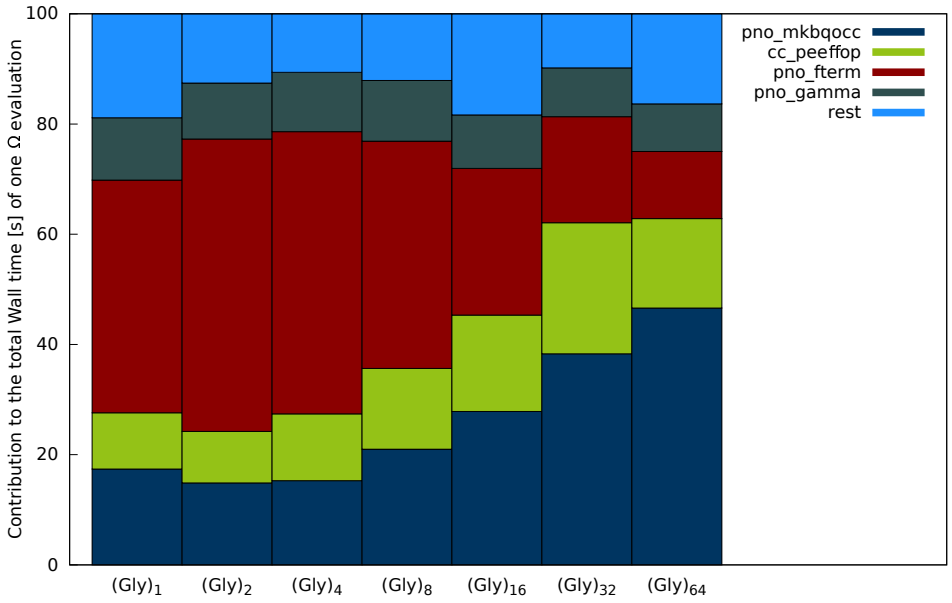
During the evaluation of the vector function of the cluster amplitudes and the right transformation of the Jacobi matrix, the matrix elements of the environmental coupling operator are computed. For the Gly_{64} system, the evaluation of the $\tilde{G}^{\Delta}(\mathbf{D}^{\Delta})$ matrix is slightly more expansive ($\sim 940\,\mathrm{s}$), than the corresponding term containing the transition density $\tilde{G}^{\Delta}(\mathbf{D}^{\nu})$ ($\sim 760\,\mathrm{s}$). However, even by subtracting of these contributions to the total wall time, the Ω evaluation is roughly twice as costly than the σ^{R} transformation. The reason for this is that the PNO basis scales linear with the system size for the ground state, while the scaling is linear with respect to the chromophore size for excited states.[33] Since the character of the first transition of Gly_{64} is a charge transfer from the terminal carboxyl group to the terminal ammonium group, the chromophore size is small, leading to the observation that the ground state PNO basis is roughly 120 times larger the corresponding excited state PNO basis.

In order to investigate the contributions of the $\tilde{G}$ matrix element evaluation to the total wall time of the Ω and σ^{R} construction, the timings of called subroutines were taken during the calculation of the first transition of the Glycinechains. The contributions of the most time-consuming subroutine calls are depicted in Figure 5.6. Nearly for all system sizes at least 80 % of the total wall time was spent in the subroutines cc_peeffop, pno_mkbqocc, pno_fterm and pno_gamma. Concerning the Ω evaluation, the computational costs for rather small Glycine chains (Gly_1-Gly_8) are dominated by the computation of the F-Term Ω^{F}, which is performed in the subroutine pno_fterm. Here, a contribution of $\sim 41\,\%$ for the Gly_8 system was obtained. Within the pno_fterm, the sum over T_1-dressed two-electron integrals $\hat{K}^{ij}_{\bar{a}_{ij}\bar{b}_{ij}}$ in the PNO basis, that yield the Ω^{F} term, are evaluated, together with the corresponding C intermediates to build these integrals. The costs of both transformations scale linearly with the system sizes for sufficient large chains[33]. Therefore, with increasing chain length the computational cost for the construction of the half-transformed 3-index integrals

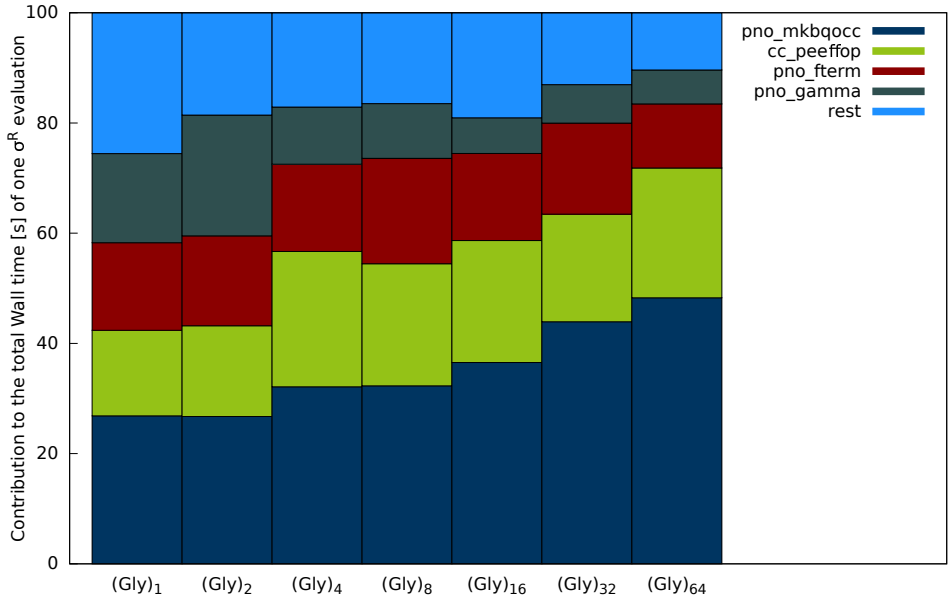
$$(Q_i|\nu\hat{i}) = (Q_i|\nu\mu)\Lambda^h_{\mu i}, \tag{5.5}$$

which is performed in the subroutine pno_mkbqocc is the dominant contribution ($\sim 47\,\%$ in the case of Gly_{64}). Regarding the construction of the $\tilde{G}$ matrix elements, that is performed in the subroutine cc_peeffop, the contribution amounts to $\sim 16\,\%$ for the largest Glycinechaine and about $\sim 15\,\%$ for the smaller Gly_8 system and are thus more than half the amount of the corresponding dominant contributions. The same tendency can be observed for the evaluation of the right transformation σ^{R}. Here, the evaluation of $\tilde{G}^{\Delta}(\mathbf{D}^{\nu})$

contributes to $\sim 22\,\%$ to the Gly_8 and $24\,\%$ to the largest system under consideration. For the Gly_{64} chain, the largest part to the total wall time of one right transformation is contributed by the subroutine pno_mkbqocc. In this subroutine roughly twice as much time was spent than in the subroutine cc_peeffop. Thus the evaluation of the matrix elements of the environmental coupling operator does not represent a dominant time contribution to the total wall time of a Ω and σ^{R} evaluation.



(a)



(b)

Figure 5.6: Contributions (in %) to the total wall time of the most significant called subroutines during the Ω (a)) and a σ^{R} (b)) evaluation using the COSMO-PNO-CC2 scheme.

5.4 Application of COSMO-PNO-CC2 to Rylenediimides

In this section, the applicability of the current COSMO-PNO-CC2 implementation for the computation of solvent effects on vertical excitation energies of large molecular systems should be demonstrated. For this purpose, unsubstituted and bay-substituted rylenediimides[88,89] were chosen. This family of organic compounds can be seen as aromatic polymeric systems, in which the monomer is represented by a naphthalene molecule. Rylene are formally obtained by condensation of two or more naphthalene units in peri position, such that two adjacent naphthalen units are connected by two C-C bonds. In one often used synthesis route, these molecular systems are obtained as diimides[90], where the two diimide groups are situated at both ends of the planar conjugated pi system. The general structure of these rylenediimides are depicted in Figure 5.7. Up to now, unsubstituded rylenediimides (R=H) are obtained up to six naphthalene units[91], leading to a systematical enlargement of the pi system. Due to their remarkable photophysical properties, like high fluorescence quantum yields[92], high photostability[93] and high extinction coefficients[92], rylene are used in a variety of applications, such as light-emitting diodes and photovoltaic[94] and optoelectronic[94] technologies.
Exploiting the high fluorescence quantum yields in combination with the non-toxicity[95] of rylenes for the labeling of biological systems[95,96] within the use of single-molecular spectroscopy[97] make it necessary to introduce hydrophilic functionalities to the hydrophobic rylene dyes. Two possible positions for the functionalization were recognized: the nitrogen atom of the imide structure and the bay region, that is the position perpendicular to the molecular axis, of the π system. Since functionalization of the imide groups comes along with a reduction of the fluorescence quantum yield[98], the bay functionalization represents the most beneficial position to introduce hydrophilic groups. Several bay-substituted water-soluble rylenes were synthesized, while among those the 4-sulfonylphenoxy substi-

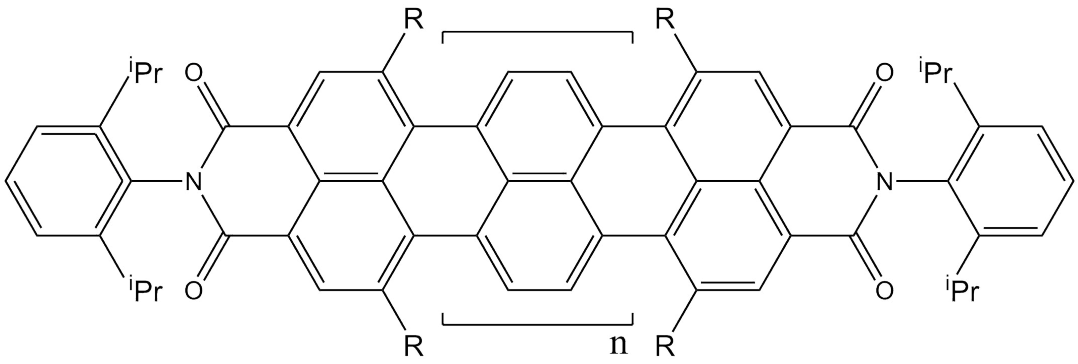


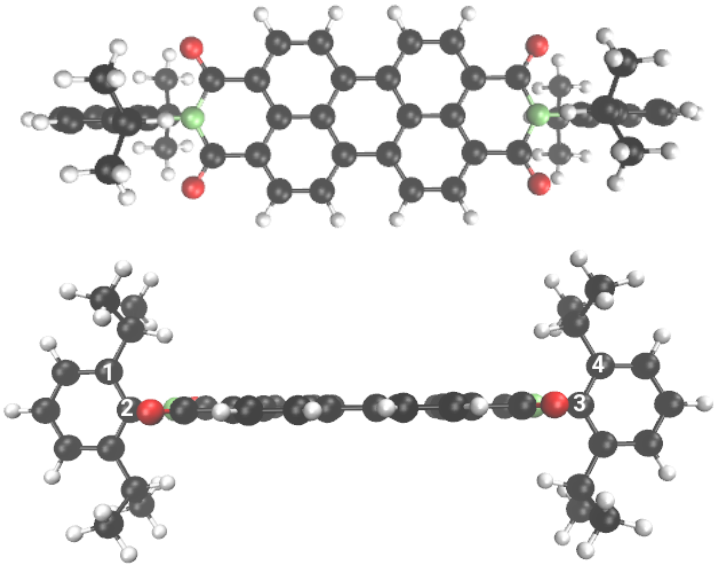
Figure 5.7: General structure of rylenediimides. For n=0 the Perrylendiimide (PDI), n=1 the Terrylendiimide (TDI) and n=2 the Quaterrylendiimide (QDI) are obtained. Functionalization in the bay-position by R=-O-Ph-SO_3^- lead to water-soluble rylenes WS-PDI (n=0) and WS-TDI (n=1).

tuted rylenes were intensively studied by means of photophysical properties in protic (water) and aprotic media (DMSO).[95,96,99,100]
In the following, the UV/VIS spectra of N,N-(2,6-diisopropylphenyl)-perylene-3,4:9,10-tetracarboxidiimide[90] (PDI) and N,N-(2,6-diisopropylphenyl)-terrylene-3,4:11,12-tetracarboxidiimide (TDI) in $CHCl_3$ (ϵ_r=4.89, n_D=1.446)[75], N,N-(2,6-diisopropylphenyl)-quaterrylene-3,4:13,14-tetracarboxidiimide[90] (QDI) in CH_2Cl_2 (ϵ_r=9.02, n_D=1.424)[75] were computed with the COSMO-PNO-CC2 approach using the aug-cc-pVDZ[72] basis set. Furthermore, the UV/VIS spectra of two water-soluble bay-substituated rylenes are considered: 1,6,7,12-tetra(4-sulfonylphenoxy)-N,N-(2,6-diisopropylphenyl)-perylene-3,4:9,10-tetracarboxidiimide (WS-PDI) in DMSO and water[95,96,99], such as 1,6,9,14-tetra(4-sulfonylphenoxy)-N,N-(2,6-diisopropylphenyl)-terrylene-3,4:11,12-tetracarboxidiimide (WS-TDI) in DMSO[100], computed with the same approach as mentioned above. Since the current PNO-CC2 and COSMO-PNO-CC2 approach do not include oscillator strengths, the assignment of the transitions is based on a comparison of the computed and experimental transition energies. The structures of all molecules were optimized in the corresponding solvent by the COSMO-B3-LYP[66,67] using the def2-TZVP[101] basis set. Start structures of PDI, TDI and QDI were taken from ref[33], in which the vertical excitation energies of these rylenes were investigated in the vacuum by using the PNO-CC2 method. Furthermore, it should be noted, that all transitions analyzed in the following, depict local $\pi\pi^*$ transitions and it can be assumed that the slower convergence obtained for CT processes in B30 and DBQ are not existent for these transitions.

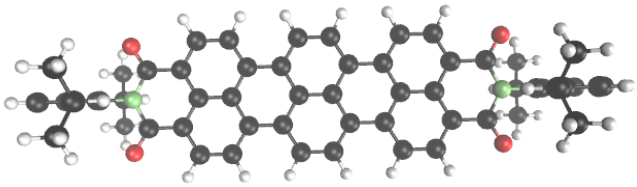
5.4.1 Unsubstituted Rylenes

An important structural feature of rylene dyes is the twist of the planar π core, which occurs mainly in bay-substituted rylene molecules. However, as was shown by structure optimizations based on the B3-LYP/def2-TZVP approach, the S-QDI molecule is slightly twisted by 6.3°, in contrast to the larger analogs: for TDI and QDI an angle of 0.7° and 0.9° was reported, respectively.[33] Here, the twist is defined as dihedral angle between the two phenyl moieties attached to the nitrogen of the imide group (see Figure 5.8). It was argued that the larger twist of the PDI π core has its origin in the interaction between the two adjacent diisopropyl groups, which are closer together in the PDI molecule.[33] For the COSMO calculations slightly smaller twists of the planar cores were obtained (5.1° for PDI, 0.3° for TDI and QDI).
The experimental absorption spectra of PDI, TDI and QDI consists mainly of the bright $S_0 \rightarrow S_1$ transition.[90,92] Beside the 0-0 transition, the spectra of these chromophores contains a vibronic fine structure, i.e. the spectra contains information about the 0-1 and 0-2 transition.[88] The experimental 0-0 excitation energies for the $S_0 \rightarrow S_1$ transition of PDI and QDI in CH_2Cl_2 and TDI in CH_2Cl_2 are summarized in Table 5.4, together

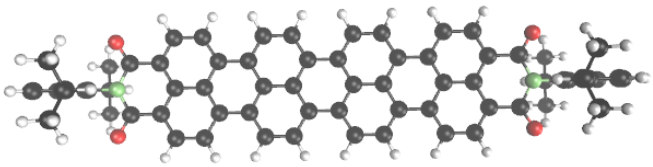
with the COSMO-PNO-CC2 and COSMO-PNO-CIS(D) energies, such as the PNO-CC2 results taken from ref[33]. When considering the experimental transition energies, a red-shift with increasing system size can be observed. Here, the $S_0 \rightarrow S_1$ energy amounts to 2.42 eV in the case of PDI, while the this transition is red-shifted by 0.8 eV for the QDI chromophore. The red-shift in connection with the extension of the π-conjugated planar scaffold can be explained with the simple particle in the box model, in which the energy difference between two states depends on the inverse of the squared box size.[91]
The energies obtained by the COSMO-PNO-CC2 approach are in good agreement with respect to the experimental data. Here, the largest deviation to the experiment is only of about 0.08 in the case of the QDI molecule. However, the description of solvent



(a)



(b)



(c)

Figure 5.8: COSMO-B3-LYP/def2-TZVP optimized structures of: a) and b) PDI, c) and d) TDI, e) and f) QDI. The twisting angle is defined as dihedral angle between the two diisopropylphenylgroups (see numbered C-atoms in b))

effects by COSMO, neglects beside possible hydrogen bonds between the CH_2Cl_2 or $CHCl_3$ solvent molecules and the carbonyl groups of the diimide moieties, the more important dispersion interactions. This interaction is especially for large extended aromatic systems as the rylene chromophores of particular importance. Thus, the good agreement with the experimental data can be a fortunate error compensation between the error in neglecting the important dispersion forces by COSMO and the intrinsic CC2 error.

Table 5.4: Experimental[90,92] and computed 0-0 transitions of the rylenes PDI, TDI and QDI. Computed energies are presented for the COSMO-PNO-CC2 and COSMO-PNO-CIS(D) approach using the aug-cc-pVDZ basis set. Transition energies obtained with the PNO-CC2/aug-cc-pVDZ approach were taken from ref[33].

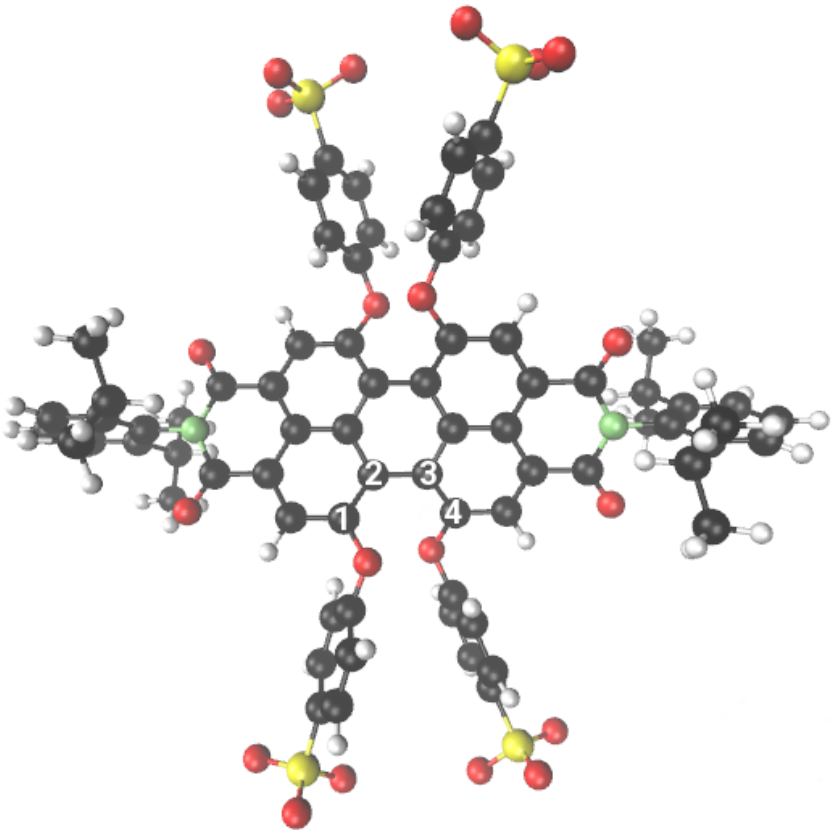
Rylene	Solvent	Exp.	PNO-CC2[33]	COSMO-PNO-CC2	COSMO-PNO-CIS(D)
PDI	CH_2Cl_2	2.42[90]	2.59[33]	2.42	2.65
TDI	$CHCl_3$	1.91[92]	2.09[33]	1.87	2.09
QDI	CH_2Cl_2	1.62[90]	-	1.54	1.75

5.4.2 Bay-Substituted Rylenes

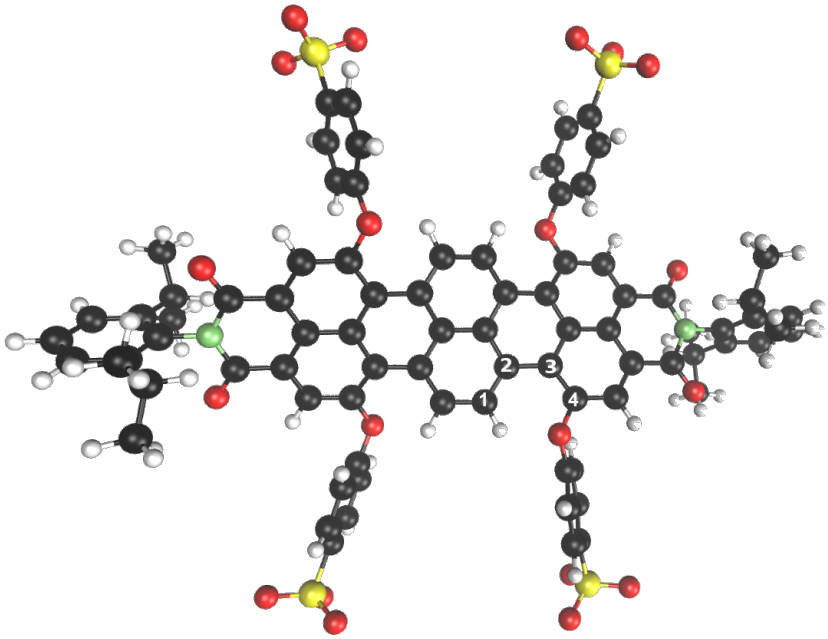
The bay-substituted rylenes WS-PDI and WS-TDI are functionalized by 4-sulfonylphenoxy groups. Due to the relatively high acidity of the sulfonyl groups in water the sulfonyl groups can be seen as completely deprotonated, as can be concluded by considering the pK_a value of the analouge compound benzenesulfonic acid[102] (pK_a=-2.8). For the solvent DMSO, only a pK_a value for the analogue compound Me-SO2-OH is reported (pK_a=1.6[103]). However, the 4-sulfonylphenoxy pK_a should be lower than the corresponding value of Me-SO2-OH, due to the additional stabilization of the deprotonated species through the phenoxy group, justifying also the consideration of completely deprotonated sulfonyl groups. Thus, the structures of ws_pdi and ws_tdi are considered in their fully deprotonated form.
In Table 5.5 important structure parameters of the COSMO-B3LYP optimized structures of WS-PDI and WS-TDI are summarized. Based on the COSMO-DFT calculations,

Table 5.5: Structure parameter of optimized WS-PDI and WS-PDI structures by COSMO-B3LYP and B3LYP calculations using the def2-TZVP basis set. θ_{Bay} is defined in Figure

Rylene	Solvent	$r(O_{Bay}\text{-}O_{Bay})$	$r_{min}(O_{Sulf}\text{-}O_{Sulf})$	θ_{Core}	θ_{Bay}
WS-PDI (eq.)	vacuum	2.6	10.8	20.6	32.3
	DMSO	2.5	4.3	34.7	30.1
	water	2.6	4.1	37.8	29.9
WS-PDI (Conf. 2)	DMSO	2.5	4.1	3.3	24.5
WS-TDI (eq.)	DMSO	6.6	7.4	50.9	19.2



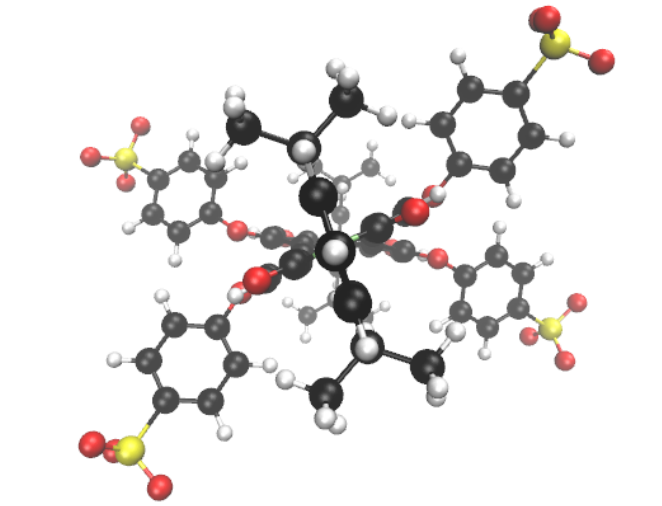
(a)



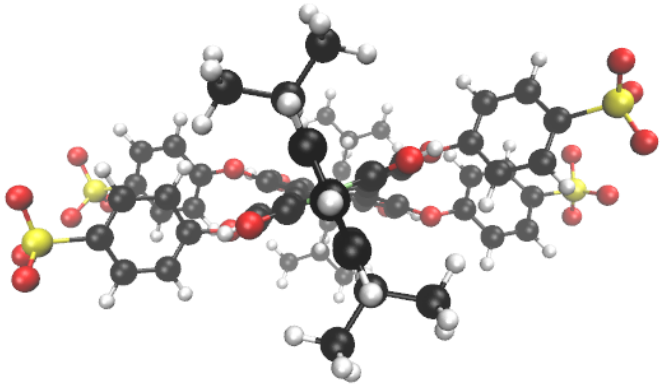
(b)

Figure 5.9: View on the π system of COSMO-B3LYP/def2-TZVP optimized equilibrium structures of WS-PDI a) and WS-TDI b). The bay dihedral angel θ_{Bay} is defined by the numbered C-atoms.

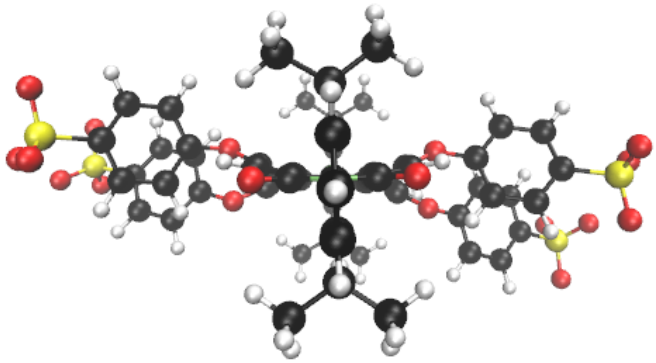
which approximate the solvent effects of DMSO, the equilibrium structure of the fully deprotonated WS-PDI and WS-TDI species are characterized by almost parallel adjacent phenoxygroups (see Figure 5.10 b)).
The bay substituents are linked through sp^3-hybridized oxygen atoms to the π core and can therefore not conjugate to the rylene π system. Especially in the case of WS-PDI, it can be found that the oxygen atoms at the bay position are relatively close to each other (2.5). This results in a twist of the polynapthalene core by roughly 35°. A larger twist was found for the water-soluble terrylenediimide (51°), which is more flexible due to the larger π system. For the WS-PDI chromophore also a conformer $8.22\,\mathrm{mol}^{-1}$ higher in energy was found (see 5.10 c)). This confomer is characterized by nearly no twist (3.3°) since the adjacent bay oxygen atoms avoid each other in a way that is symmetric with respect to the oxygen atoms on the other side of the π system. Furthermore, also a vacuum structure was optimized by B3LYP/def2-TZVP (see 5.10 a)). The SO_3^- groups of this structure are separated by more than twice the distance of the COSMO equilibrium structure. Due to the electrostatic field arising from the solvents molecules, described by the cavity charges in the conductor-like screening model, the charged groups can approach each other, more than in the vacuum case, while the π system is twisted to a larger extent: $\sim 35°$ for DMSO vs. $\sim 20°$ in vacuum.
In contrast to the unsubstituted rylenes, whose UV/VIS spectra contain mainly information about the $S_0 \rightarrow S_1$ transition, the spectra of the WS-PDI and WS-TDI chromophores contain also a broad peak in the region of $\sim 2.75\,\mathrm{eV}$ which is associated to the $S_0 \rightarrow S_2$ transition. Considering the experimental data measured in DMSO (see Table 5.6), the first transition of the water-soluble rylenes is red-shifted in comparison to the anolouge unsubstituted rylenes (see Table 5.4). While for the PDI analogs the red-shift amounts to 0.27 eV, a considerably smaller shift was reported for the TDI analogs 0.08 eV. When considering the results of the COSMO structure optimizations, the larger red-shift for the smaller rylene is remarkable, since the WS-TDI chromophore was more twisted than the WS-PDI rylene and structural effects on the transitions can be seen as one of the important factors for the red-shift.
The transition energies obtained by the COSMO-PNO-CC2/aug-cc-pVDZ calculations are presented in Table 5.6. The theoretical $S_0 \rightarrow S_1$ energies are in good agreement with the experimental values, as was already observed for the unsubstituted rylenes. The largest deviation to the experiment amouts about $\sim 0.05\,\mathrm{eV}$, for WS-TDI in water. However, it should be noted at this point, that due to the large π system, WS-PDI and WS-TDI tend to self-associate due to $\pi - \pi$ stacking in protic solvents like water, while these chromophores are mainly monomeric in DMSO.[99,100]
For the second prominent peak of the absorptions spectra in DMSO only a range could be extracted from the provided data in ref.[99,100] for both rylenes. This range is estimated as 2.7 eV–3.0 eV and 2.8 eV–3.1 eV for WS-PDI and WS-TDI, respectively. Based on the



(a)



(b)



(c)

Figure 5.10: View along the molecular axis of B3LYP/def2-TZVP (a)) and COSMO-B3LYP/def2-TZVP (b) and c)) optimized structures of WS-PDI. In the vacuum structure a) the distance between the sulfonyl groups are larger than in the COSMO equilibrium structure b). The COSMO structure c) contains in comparison to b) and a) nearly no twist.

COSMO-PNO approach two transitions, i.e. the $S_0 \rightarrow S_2$ and $S_0 \rightarrow S_3$ transitions, lie in the experimental range for the second prominent feature of the experimental spectrum. Here, for WS-PDI nearly degenerated states in the region of 2.9 eV were computed. For WS-TDI these states are separated by roughly 0.25 eV and amount to 2.76 eV and 3.01 eV. Thus also the high-energy region of the spectra could be well reproduced by the implemented COSMO-PNO approach.

Table 5.6: Experimental[95,96,99] and computed 0-0 transitions of the bay-substituted rylenes WS-PDI and WS-TDI in water and DMSO. For the theoretical examination of these transitions COSMO-PNO-CC2 calculations with the aug-c-pVDZ basis set were performed with a PNO threshold of 10^{-8}

		DMSO		Water	
Rylene	Transition	Exp.	CC2	Exp.	CC2
ws_pdi	$S_0 \rightarrow S_1$	2.15[99]	2.18	2.18[96]	2.23
	$S_0 \rightarrow S_2$	2.7-3.0[99]	2.88	2.73[96]	2.90
	$S_0 \rightarrow S_3$	-	2.89	-	2.90
ws_tdi	$S_0 \rightarrow S_1$	1.83[100]	1.85		
	$S_0 \rightarrow S_2$	3.1-2.8[100]	2.76		
	$S_0 \rightarrow S_3$	-	3.01		

6 Summary & Outlook

In this thesis, the second-order approximate coupled cluster singles and doubles model in its pair natural orbital implementation has been combined with the conductor-like screening model, such as the polarizable embedding scheme to account for environmental effects on vertical transition energies obtained within linear response theory. For both solvation models the post-SCF reaction field was used, that account for correlation effects on the mutual polarization between the solute and solvent only by the single excitation parts of the wavefunction parameters.

The correctness of the COSMO- and PE-PNO-CC2 implementation was confirmed with respect to the canonical implementation on small molecules by switching off all approximations coupled to the PNO threshold and using the whole virtual space for each pair. Furthermore, it was shown for the COSMO-PNO-CC2 scheme, that in the case of long-range charge transfer processes, as they occur in the compounds DBQ and B30, a slower convergence of the truncation errors can be expected, in comparison to the vacuum PNO-CC2 calculations. This is due to the fact that the environment effects enhance the charge transfer within the solute molecule upon excitation. For all other considered organic molecules, the convergence of the COSMO truncation errors tends to be similar to the vacuum case. Here, an error of or below $\sim 0.01\,\mathrm{eV}$ was obtained for a threshold of 10^{-8}. Considering the computational cost, it was shown that the Ω, $\bar{t} \cdot A$ and $A \cdot b$ evaluations were too time demanding for systems including ~ 4000 AOs, using the canoncial $\mathcal{O}(\mathcal{N})^5$ scaling COSMO-CC2 implementation and a smp parallelization with 20 processors. On the other hand, the COSMO-PNO-CC2 implementation leads to a reduced scaling of all mentioned steps ($\mathcal{O}(\mathcal{N}^3)$). Most importantly it could be shown that the COSMO contributions, which are computed during the Ω and $A \cdot b$ steps do not dominate the computational costs, even for the largest system considered.

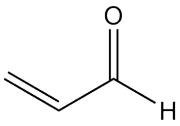
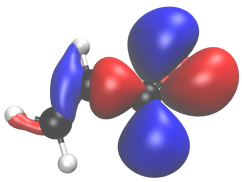
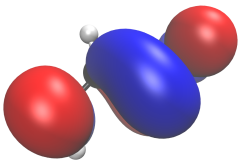
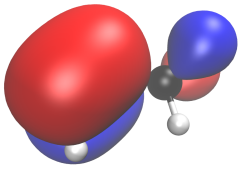
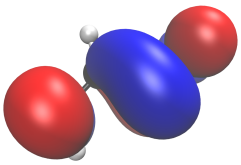
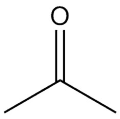
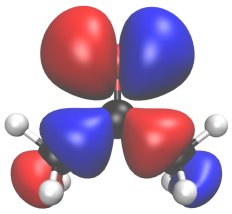
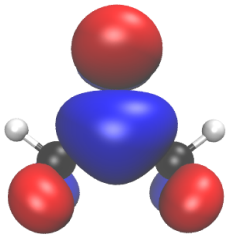
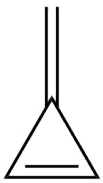
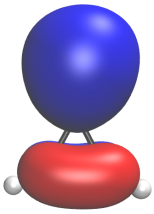
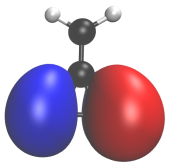
Lastly, the $S_0 \rightarrow S_1$ transition of unsubstituted and bay-substituted rylenediimides in different solvents were computed based on the implemented COSMO-PNO-CC2 scheme. Here, the obtained transition energies are in close agreement with the experimental data, while the deviation is lower than $\sim 0.1\,\mathrm{eV}$. However, the good agreement might be a error compensation between the intrinsic CC2 error and the neglection of the dispersion effects through the COSMO approach.

Regarding further work, on the COSMO- and PE-PNO-CC2 implementation a re-adaption of the pair thresholds should be considered, since it has been shown that varying this pa-

rameter lead to a significant change of the truncation errors, in the case of B30 and DBQ. Furthermore, for the PE-PNO-CC2 the use of effective core potentials should be implemented and tested on selected test chromophores. In addition, for molecules with significant correlation contributions from the single excitation part of the CC wavefunction, a way to re-optimize the MP1-PNOs during the solution of the ground state equations should be considered, in a way that these single amplitudes are included. Moreover, the implementation of oscillator strengths should be targeted within the `pnoccsd` program to predict the full absorption spectra of organic molecules.

7 Appendix

Table 7.1: Occupied and virtual natural orbitals (NTOs) of the in section 5.2.1 investigated local excitations of acrolein, acetone and MCP.

Name	Str. Formula	Char.	$\#_{\text{Vac}}$	$\#_{\text{Sol}}$	occ. NTO	vir. NTO
Acrolein		$n\pi^*$	S_1	S_1		
		$\pi\pi^*$	S_4	S_2		
Acetone		$n\pi^*$	S_1	S_1		
Methylene-cyclopropene (MCP)		$\pi\pi^*$	S_1	S_1		

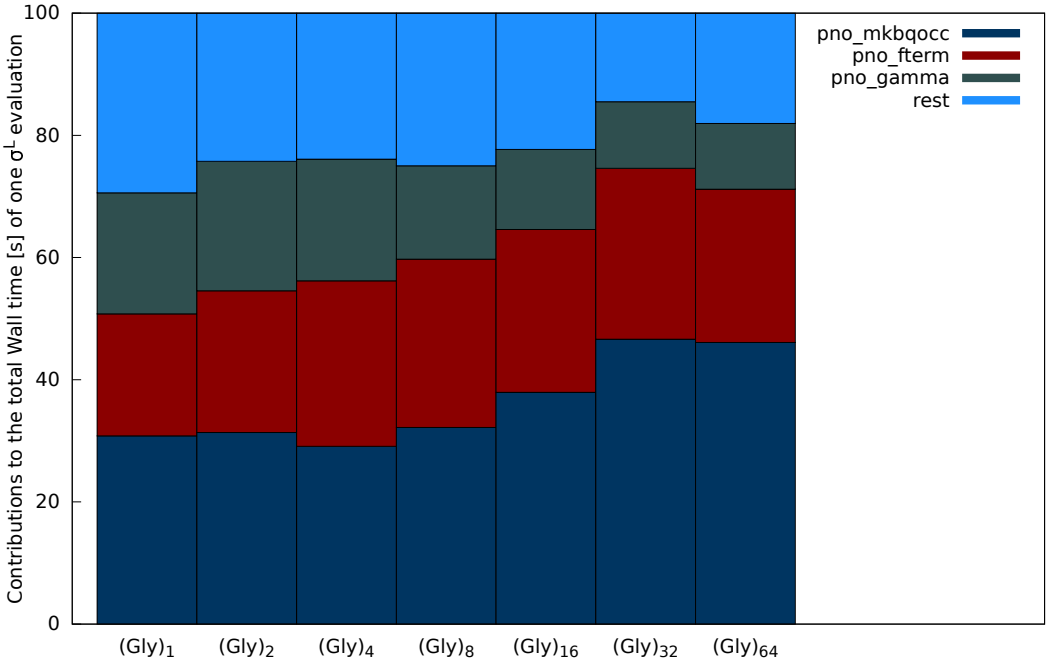


Figure 7.1: Contributions (in %) to the total wall time of the most significant called subroutines during the σ^{L} evaluation using the COSMO-PNO-CC2 scheme.

Table 7.2: Occupied and virtual natural transition orbitals (NTOs) of the in section 5.2.1 investigated charge transfer transitions of Pentadienal, Bisthiophene, DMBAN, Michler's ketone and DBQ.

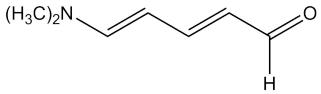
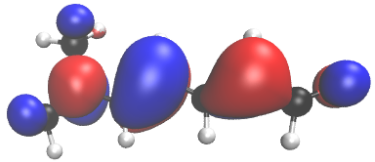
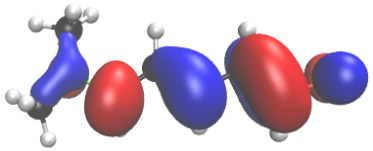
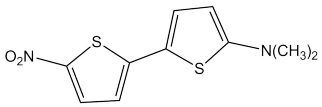
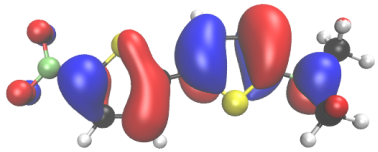
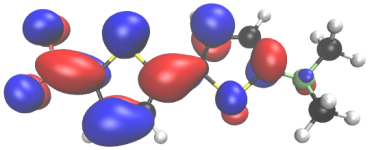
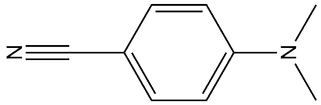
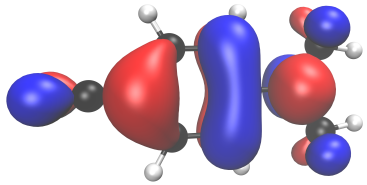
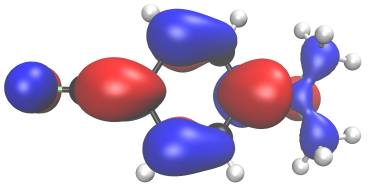
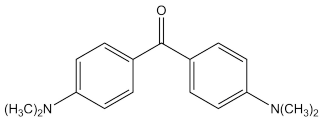
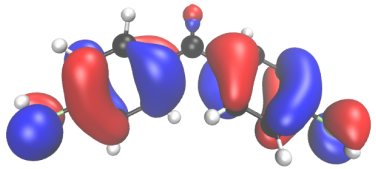
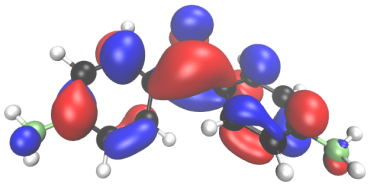
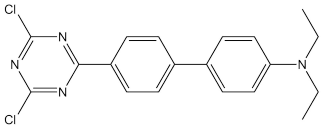
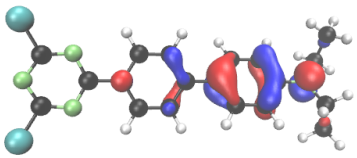
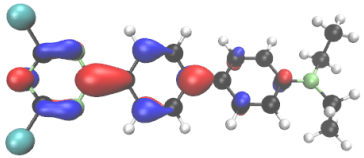
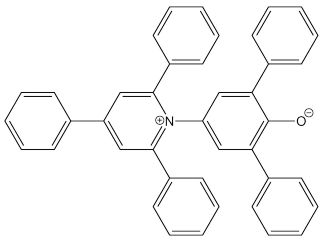
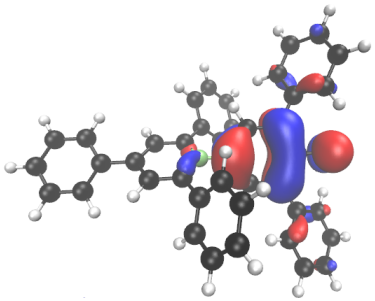
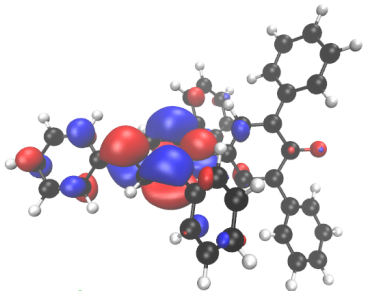
Name	Str. Formula	Char.	$\#_{Vac}$	$\#_{Sol}$	occ. NTO	vir. NTO
Pentadienal		CT	S_2	S_1		
Bisthiophene		CT	S_1	S_1		
DMBAN		CT	S_2	S_2		
Michler's ketone		CT	S_2	S_1		
DBQ		CT	S_1	S_1		
B30		CT	S_1	S_1		

Table 7.3: Vertical excitation energies (in eV) of selected transitions of acrolein and acetone in water, MCP in methanol, such as corresponding vacuum transition energies calculated for the canonical RI-CC2 and COSMO-RI-CC2 approach, such as the corresponding PNO schemes with different PNO thresholds using the aug-cc-pVTZ basis set.

				PNO-CC2					
		RI-CC2		Vaccum			COSMO		
Molecule	Char.	ω_{Vac}	ω_{COSMO}	$\omega_{10^{-4}}$	$\omega_{10^{-5}}$	$\omega_{10^{-6}}$	$\omega_{10^{-4}}$	$\omega_{10^{-5}}$	$\omega_{10^{-6}}$
Acrolein	$n\pi^*$	3.84395	4.00169	4.15085	3.92929	3.85637	4.32197	4.09166	4.01331
	$\pi\pi^*$	6.78956	6.34041	6.95939	6.84906	6.80623	6.55580	6.40318	6.35419
Acetone	$\pi\pi^*$	4.53259	4.65469	4.70987	4.61049	4.54304	4.84931	4.74160	4.66642
MCP	$\pi\pi^*$	4.49730	4.71985	4.63232	4.52752	4.50787	4.87974	4.75336	4.73200

Table 7.4: Vertical excitation energies (in eV) of selected transitions of Pentadienal and Bisthiophene in water, DMBAN in acetonitrile, DBQ in dimethylsulfoxide and Michler's ketone in formamide, such as corresponding vacuum transition energies calculated for the canonical RI-CC2 and COSMO-RI-CC2 approach, such as the corresponding PNO schemes with different PNO thresholds using the aug-cc-pVTZ basis set.

				PNO-CC2							
		RI-CC2		Vaccum				COSMO			
Molecule	Char.	ω_{Vac}	ω_{COSMO}	$\omega_{10^{-6}}$	$\omega_{10^{-7}}$	$\omega_{10^{-8}}$	$\omega_{10^{-9}}$	$\omega_{10^{-6}}$	$\omega_{10^{-7}}$	$\omega_{10^{-8}}$	$\omega_{10^{-9}}$
Pentadienal	CT	4.23068	3.60378	4.28457	4.23060	4.22311	-	3.63255	3.59513	3.59535	-
Bisthiophene	CT	3.10657	2.54363	3.25623	3.14996	3.11171	-	2.70228	2.59035	2.55260	-
DMBAN	CT	4.66537	4.33947	4.78372	4.68689	4.66908	-	4.42649	4.34994	4.33684	-
Michler's ketone	CT	4.12549	3.61418	4.38253	4.20836	4.14223	-	3.88414	3.69736	3.62908	-
DBQ	CT	3.06992	2.69383	3.28295	3.12041	3.07063	3.06383	2.97992	2.79929	2.73400	2.71396
DBQ (T_{Pair}=-1)	CT	-	-	-	-	-	-	2.90779	2.76095	2.71739	2.70647
B30	CT	1.22344	1.88096	1.11608	1.05457	1.06443	1.09294	2.19767	2.02599	1.94723	1.91561
B30 (T_{Pair}=-1)	CT	-	-	-	-	-	-	2.07903	1.96619	1.92553	-

Table 7.5: Wall time [in s] of called subroutines during a Ω evaluation using the COSMO-PNO-CC2 scheme.

Subroutine	Gly_1	Gly_2	Gly_4	Gly_8	Gly_{16}	Gly_{32}	Gly_{64}
pno_vecfun	1.087	4.389	12.895	39.454	138.153	533.824	5798.307
pno_fhatia	0.016	0.046	0.110	0.319	1.138	4.895	20.685
pno_gamma	0.123	0.445	1.386	4.345	13.395	47.281	500.832
pno_intij	0.062	0.148	0.399	1.293	4.300	15.241	374.714
pno_mkbqocc	0.189	0.653	1.970	8.285	38.468	204.455	2702.593
pno_jterm	0.032	0.084	0.268	0.847	2.940	9.995	296.615
pno_hterm	0.040	0.126	0.293	0.953	3.466	12.530	136.574
pno_osv	0.009	0.014	0.027	0.101	11.342	4.171	25.967
pno_fterm	0.459	2.329	6.605	16.270	36.787	102.715	705.460
cc_peeffop	0.111	0.410	1.563	5.779	24.142	127.015	941.180
pno_sett2res	0.035	0.098	0.171	0.377	0.760	1.626	36.130

Table 7.6: Wall time [in s] of called subroutines during a σ^{L} evaluation using the COSMO-PNO-CC2 scheme.

Subroutine	Gly_1	Gly_2	Gly_4	Gly_8	Gly_{16}	Gly_{32}	Gly_{64}
pno_lhtr	0.646	2.143	7.052	28.515	116.989	451.918	5114.547
pno_fhatia	0.020	0.046	0.113	0.339	1.126	5.318	68.237
pno_gamma	0.128	0.454	1.405	4.357	15.333	49.290	549.931
pno_intij	0.029	0.110	0.568	3.070	7.929	17.509	202.012
pno_mkbqocc	0.199	0.672	2.052	9.180	44.379	210.679	2357.050
pno_jterm	0.022	0.057	0.227	0.981	4.037	15.118	279.407
pno_hterm	0.041	0.120	0.319	0.933	3.331	14.688	189.746
pno_osv	0.012	0.016	0.031	0.558	6.582	2.489	26.014
pno_fterm	0.129	0.497	1.910	7.854	31.184	126.414	1283.787
pno_sett2res	0.042	0.096	0.199	0.384	0.774	1.616	32.185

Table 7.7: Wall time [in s] of called subroutines during a σ^{R} evaluation using the COSMO-PNO-CC2 scheme.

Subroutine	Gly_1	Gly_2	Gly_4	Gly_8	Gly_{16}	Gly_{32}	Gly_{64}
pno_rhtr	0.767	2.532	5.973	25.779	105.126	538.196	3254.100
pno_fhatia	0.024	0.058	0.134	0.400	1.307	10.184	81.311
pno_gamma	0.124	0.555	0.619	2.559	6.803	37.620	200.179
pno_intij	0.031	0.116	0.368	1.740	5.213	30.236	162.697
pno_mkbqocc	0.206	0.677	1.919	8.329	38.414	236.448	1570.787
pno_jterm	0.023	0.058	0.208	0.877	3.073	13.174	39.407
pno_hterm	0.042	0.097	0.115	0.545	1.710	2.418	4.339
pno_osv	0.013	0.019	0.037	0.117	7.183	5.338	28.261
pno_fterm	0.122	0.413	0.947	4.932	16.603	88.856	378.413
cc_peeffop	0.119	0.417	1.466	5.707	23.255	105.054	766.593
pno_sett2res	0.038	0.076	0.053	0.128	0.185	0.100	0.215

Table 7.8: Wall time [in s] of called subroutines during a Ω evaluation using the COSMO-RI-CC2 scheme.

Subroutine	Gly_1	Gly_2	Gly_4	Gly_8	Gly_{16}
ccvecfun	0.686	2.237	10.621	107.378	2274.058
ccmkboi	0.155	0.437	1.443	5.817	85.634
ccn5engine	0.231	0.783	5.209	84.381	2088.793
cc_intij	0.006	0.038	0.208	1.393	11.057
cc_gstar	0.027	0.112	0.541	3.159	27.116
cc_jgterm	0.139	0.393	1.224	4.291	18.707
cc_hterm	0.010	0.026	0.151	0.951	7.400
cc_peeffop	0.108	0.401	1.606	5.839	24.126

Table 7.9: Wall time [in s] of called subroutines during a σ^{L} evaluation using the COSMO-RI-CC2 scheme.

Subroutine	Gly_1	Gly_2	Gly_4	Gly_8	Gly_{16}
cclhtr	0.452	1.655	11.708	165.148	3785.139
ccmkboi	0.088	0.251	0.933	4.580	76.608
ccn5engine	0.089	0.571	6.631	120.187	2903.373
cc_intij	0.012	0.051	0.291	2.102	16.000
cc_gstar	0.029	0.112	0.570	3.521	29.434
cc_jgterm	0.140	0.391	1.244	4.228	18.941
cc_hterm	0.011	0.028	0.152	0.949	6.834

Table 7.10: Wall time [in s] of called subroutines during a σ^{R} evaluation using the COSMO-RI-CC2 scheme.

Subroutine	Gly_1	Gly_2	Gly_4	Gly_8	Gly_{16}
rhtr	0.736	2.586	12.667	157.529	3629.678
ccmkboi	0.094	0.263	0.971	4.900	82.240
ccn5engine	0.271	1.136	6.428	108.957	2760.363
cc_intij	0.005	0.017	0.102	0.714	5.398
cc_gstar	0.030	0.114	0.540	3.103	27.933
cc_jgterm	0.139	0.393	1.227	4.255	19.010
pno_hterm	0.011	0.027	0.149	0.939	7.024
cc_peeffop	0.106	0.402	1.519	5.646	23.635

Bibliography

[1] H. Sekino, R. J. Bartlett, *International Journal of Quantum Chemistry* **1984**, *26*, 255–265.

[2] H. Koch, P. Jo/rgensen, *The Journal of Chemical Physics* **1990**, *93*, 3333–3344.

[3] H. Koch, H. J. A. Jensen, P. Jo/rgensen, T. Helgaker, *The Journal of Chemical Physics* **1990**, *93*, 3345–3350.

[4] J. Čížek, *The Journal of Chemical Physics* **1966**, *45*, 4256–4266.

[5] G. D. Purvis, R. J. Bartlett, *The Journal of Chemical Physics* **1982**, *76*, 1910–1918.

[6] J. Noga, R. J. Bartlett, *The Journal of Chemical Physics* **1987**, *86*, 7041–7050.

[7] S. A. Kucharski, R. J. Bartlett, *The Journal of Chemical Physics* **1992**, *97*, 4282–4288.

[8] H. Koch, O. Christiansen, P. Jo/rgensen, A. M. Sanchez de Merás, T. Helgaker, *The Journal of Chemical Physics* **1997**, *106*, 1808–1818.

[9] H. Koch, O. Christiansen, P. Jørgensen, J. Olsen, *Chemical Physics Letters* **1995**, *244*, 75 – 82.

[10] O. Christiansen, H. Koch, P. Jørgensen, *Chemical Physics Letters* **1995**, *243*, 409 – 418.

[11] P. Hohenberg, W. Kohn, *Phys. Rev.* **1964**, *136*, B864–B871.

[12] W. Kohn, L. J. Sham, *Phys. Rev.* **1965**, *140*, A1133–A1138.

[13] N. Mardirossian, M. Head-Gordon, *Molecular Physics* **2017**, *115*, 2315–2372.

[14] S. Grimme, J. Antony, S. Ehrlich, H. Krieg, *The Journal of Chemical Physics* **2010**, *132*, 154104.

[15] S. Grimme, S. Ehrlich, L. Goerigk, *Journal of Computational Chemistry* **2011**, *32*, 1456–1465.

[16] T. Yanai, D. P. Tew, N. C. Handy, *Chemical Physics Letters* **2004**, *393*, 51 – 57.

[17] A. D. Laurent, D. Jacquemin, *International Journal of Quantum Chemistry* **2013**, *113*, 2019–2039.

[18] F. London, *Zeitschrift für Physik* **1930**, *63*, 245–279.

[19] P. Pulay, *Chemical Physics Letters* **1983**, *100*, 151 – 154.

[20] S. Saebo, P. Pulay, *Annual Review of Physical Chemistry* **1993**, *44*, 213–236.

[21] P. Pulay, S. Saebø, *Theoretica chimica acta* **1986**, *69*, 357–368.

[22] S. Sæbø, P. Pulay, *Chemical Physics Letters* **1985**, *113*, 13 – 18.

[23] P. Pulay, S. Saebø, *Theoretica chimica acta* **1986**, *69*, 357–368.

[24] S. Saebo/, P. Pulay, *The Journal of Chemical Physics* **1987**, *86*, 914–922.

[25] S. Saebo, P. Pulay, *The Journal of Chemical Physics* **1988**, *88*, 1884–1890.

[26] B. Helmich, C. Hättig, *The Journal of Chemical Physics* **2013**, *139*, 084114.

[27] M. S. Frank, C. Hättig, *The Journal of Chemical Physics* **2018**, *148*, 134102.

[28] C. Riplinger, F. Neese, *The Journal of Chemical Physics* **2013**, *138*, 034106.

[29] J. Yang, Y. Kurashige, F. R. Manby, G. K. L. Chan, *The Journal of Chemical Physics* **2011**, *134*, 044123.

[30] W. Meyer, *International Journal of Quantum Chemistry* **1971**, *5*, 341–348.

[31] G. Schmitz, B. Helmich, C. Hättig, *Molecular Physics* **2013**, *111*, 2463–2476.

[32] B. Helmich, C. Hättig, *The Journal of Chemical Physics* **2011**, *135*, 214106.

[33] B. Helmich-Paris, PhD thesis, Ruhr-Universität Bochum, **2014**.

[34] K. Sneskov, T. Schwabe, O. Christiansen, J. Kongsted, *Phys. Chem. Chem. Phys.* **2011**, *13*, 18551–18560.

[35] J. M. Olsen, K. Aidas, J. Kongsted, *Journal of Chemical Theory and Computation* **2010**, *6*, 3721–3734.

[36] T. Schwabe, K. Sneskov, J. M. Haugaard Olsen, J. Kongsted, O. Christiansen, C. Hättig, *Journal of Chemical Theory and Computation* **2012**, *8*, 3274–3283.

[37] D. Hršak, A. Marefat Khah, O. Christiansen, C. Hättig, *Journal of Chemical Theory and Computation* **2015**, *11*, 3669–3678.

[38] K. Sneskov, T. Schwabe, J. Kongsted, O. Christiansen, *The Journal of Chemical Physics* **2011**, *134*, 104108.

[39] A. Marefat Khah, S. Karbalaei Khani, C. Hättig, *Journal of Chemical Theory and Computation* **2018**, *14*, 4640–4650.

[40] J. Tomasi, B. Mennucci, R. Cammi, *Chemical Reviews* **2005**, *105*, 2999–3094.

[41] S. Miertuš, E. Scrocco, J. Tomasi, *Chemical Physics* **1981**, *55*, 117–129.

[42] A. Klamt, G. Schüürmann, *J. Chem. Soc. Perkin Trans. 2* **1993**, 799–805.

[43] M. Caricato, G. Scalmani, G. W. Trucks, M. J. Frisch, *The Journal of Physical Chemistry Letters* **2010**, *1*, 2369–2373.

[44] M. Caricato, *The Journal of Chemical Physics* **2011**, *135*, 074113.

[45] M. Caricato, *The Journal of Chemical Physics* **2018**, *148*, 134113.

[46] M. Caricato, *ChemPhotoChem* **2019**, *3*, 747–754.

[47] B. Lunkenheimer, A. Köhn, *Journal of Chemical Theory and Computation* **2013**, *9*, 977–994.

[48] S. Karbalaei Khani, A. Marefat Khah, C. Hättig, *Phys. Chem. Chem. Phys.* **2018**, *20*, 16354–16363.

[49] F. del Valle, J. Tomasi, *Chemical Physics* **1991**, *150*, 139 – 150.

[50] O. Christiansen, *Theoretical Chemistry Accounts* **2006**, *116*, 106–123.

[51] T. Helgaker, P. Jørgensen, J. Olsen, *Molecular Electronic Structure Theory*, John Wiley & Sons, LTD, Chichester, **2000**.

[52] *TURBOMOLE V7.3 2018, a development of University of Karlsruhe and Forschungszentrum Karlsruhe GmbH, 1989-2007, TURBOMOLE GmbH, since 2007; available from* `http://www.turbomole.com`.

[53] A. Stone, *The theory of intermolecular forces*, Oxford University Press, Chichester, **2013**.

[54] A. Klamt in *28th European Symposium on Computer Aided Process Engineering, Vol. 43* (Eds.: A. Friedl, J. J. Klemeš, S. Radl, P. S. Varbanov, T. Wallek), Elsevier, **2018**, p. 9.

[55] C. Hättig, F. Weigend, *The Journal of Chemical Physics* **2000**, *113*, 5154–5161.

[56] S. Corni, R. Cammi, B. Mennucci, J. Tomasi, *The Journal of Chemical Physics* **2005**, *123*, 134512.

[57] F. Neese, F. Wennmohs, A. Hansen, *The Journal of Chemical Physics* **2009**, *130*, 114108.

[58] M. Head-Gordon, R. J. Rico, M. Oumi, T. J. Lee, *Chemical Physics Letters* **1994**, *219*, 21 – 29.

[59] G. Schmitz, C. Hättig, D. P. Tew, *Phys. Chem. Chem. Phys.* **2014**, *16*, 22167–22178.

[60] J. Kongsted, A. Osted, K. V. Mikkelsen, O. Christiansen, *The Journal of Physical Chemistry A* **2003**, *107*, 2578–2588.

[61] R. J. Bartlett, G. D. Purvis, *International Journal of Quantum Chemistry* **1978**, *14*, 561–581.

[62] P. Pulay, *Chemical Physics Letters* **1980**, *73*, 393 – 398.

[63] P. Pulay, *Journal of Computational Chemistry* **1982**, *3*, 556–560.

[64] M. Häser, R. Ahlrichs, *Journal of Computational Chemistry* **1989**, *10*, 104–111.

[65] M. Von Arnim, R. Ahlrichs, *Journal of Computational Chemistry* **1998**, *19*, 1746–1757.

[66] A. D. Becke, *The Journal of Chemical Physics* **1993**, *98*, 5648–5652.

[67] C. Lee, W. Yang, R. G. Parr, *Phys. Rev. B* **1988**, *37*, 785–789.

[68] G. Knizia, *Journal of Chemical Theory and Computation* **2013**, *9*, 4834–4843.

[69] E. S. Sachs, J. Hinze, N. H. Sabelli, *The Journal of Chemical Physics* **1975**, *62*, 3393–3398.

[70] S. P. A. Sauer, M. Schreiber, M. R. Silva-Junior, W. Thiel, *Journal of Chemical Theory and Computation* **2009**, *5*, 555–564.

[71] M. Schreiber, M. R. Silva-Junior, S. P. A. Sauer, W. Thiel, *The Journal of Chemical Physics* **2008**, *128*, 134110.

[72] R. A. Kendall, T. H. Dunning, R. J. Harrison, *The Journal of Chemical Physics* **1992**, *96*, 6796–6806.

[73] F. Weigend, A. Köhn, C. Hättig, *The Journal of Chemical Physics* **2002**, *116*, 3175–3183.

[74] M. Caricato, *The Journal of Chemical Physics* **2013**, *139*, 044116.

[75] J. P. Cerón-Carrasco, D. Jacquemin, C. Laurence, A. Planchat, C. Reichardt, K. Sraïdi, *Journal of Physical Organic Chemistry* **2014**, *27*, 512–518.

[76] K. Inuzuka, *Bulletin of the Chemical Society of Japan* **1961**, *34*, 729–732.

[77] W. F. Forbes, R. Shilton, *Journal of the American Chemical Society* **1959**, *81*, 786–790.

[78] C. Reichardt, *Solvents and Solvent Effects in Organic Chemistry*, Wiley-VCH, **2003**.

[79] S. W. Staley, T. D. Norden, *Journal of the American Chemical Society* **1984**, *106*, 3699–3700.

[80] S. Dähne, F. Shob, K.-D. Nolte, *Z. Chem.* **1973**, *13*, 471–473.

[81] F. Effenberger, F. Würthner, *Angewandte Chemie International Edition in English* **1993**, *32*, 719–721.

[82] S. Spange, D. Keutel, *Liebigs Annalen der Chemie* **1992**, *1992*, 423–428.

[83] Y. Ma, R. Hao, G. Shao, Y. Wang, *The Journal of Physical Chemistry A* **2009**, *113*, 5066–5072.

[84] L. Goerigk, S. Grimme, *The Journal of Chemical Physics* **2010**, *132*, 184103.

[85] M. Rückert, *In-depth practicle No. III: Examination of the HOMO - LUMO transition of Betaine 30 on th ebasis of coupled-cluster response theory* **2018**.

[86] F. Bureš, *RSC Adv.* **2014**, *4*, 58826–58851.

[87] J. Pipek, P. G. Mezey, *The Journal of Chemical Physics* **1989**, *90*, 4916–4926.

[88] T. Weil, T. Vosch, J. Hofkens, K. Peneva, K. Müllen, *Angewandte Chemie International Edition* **2010**, *49*, 9068–9093.

[89] A. C. Grimsdale, K. Müllen, *Angewandte Chemie* **2005**, *117*, 5732–5772.

[90] H. Quante, K. Müllen, *Angewandte Chemie International Edition in English* **1995**, *34*, 1323–1325.

[91] N. G. Pschirer, C. Kohl, F. Nolde, J. Qu, K. Müllen, *Angewandte Chemie* **2006**, *118*, 1429–1432.

[92] F. O. Holtrup, G. R. J. Müller, H. Quante, S. De Feyter, F. C. De Schryver, K. Müllen, *Chemistry – A European Journal* **1997**, *3*, 219–225.

[93] C. Kohl, S. Becker, K. Müllen, *Chem. Commun.* **2002**, 2778–2779.

[94] L. Zang, Y. Che, J. S. Moore, *Accounts of Chemical Research* **2008**, *41*, 1596–1608.

[95] J. Qu, C. Kohl, M. Pottek, K. Müllen, *Angewandte Chemie International Edition* **2004**, *43*, 1528–1531.

[96] A. Margineanu, J. Hofkens, M. Cotlet, S. Habuchi, A. Stefan, J. Qu, C. Kohl, K. Müllen, J. Vercammen, Y. Engelborghs, T. Gensch, F. C. De Schryver, *The Journal of Physical Chemistry B* **2004**, *108*, 12242–12251.

[97] M. Cotlet, J. Hofkens, M. Maus, T. Gensch, M. Van der Auweraer, J. Michiels, G. Dirix, M. Van Guyse, J. Vanderleyden, A. J. W. G. Visser, F. C. De Schryver, *The Journal of Physical Chemistry B* **2001**, *105*, 4999–5006.

[98] G. Schnurpfeil, J. Stark, D. Wöhrle, *Dyes and Pigments* **1995**, *27*, 339 – 350.

[99] T. Tang, J. Qu, K. Müllen, S. E. Webber, *Langmuir* **2006**, *22*, 7610–7616.

[100] C. Jung, B. K. Müller, D. C. Lamb, F. Nolde, K. Müllen, C. Bräuchle, *Journal of the American Chemical Society* **2006**, *128*, 5283–5291.

[101] F. Weigend, R. Ahlrichs, *Phys. Chem. Chem. Phys.* **2005**, *7*, 3297–3305.

[102] J. P. Guthrie, *Canadian Journal of Chemistry* **1978**, *56*, 2342–2354.

[103] F. G. Bordwell, M. Van der Puy, N. R. Vanier, *The Journal of Organic Chemistry* **1976**, *41*, 1883–1885.